Nonlocal plasticity modelling of strain localisation in stiff clays

Miguel Mánica (miguel.angel.manica@upc.edu)
Department of Civil and Environmental Engineering
Universitat Politècnica de Catalunya, Barcelona Tech, Spain

Antonio Gens (antonio.gens@upc.edu)
Department of Civil and Environmental Engineering
Universitat Politècnica de Catalunya, Barcelona Tech, Spain

Jean Vaunat (jean.vaunat@upc.edu)
Department of Civil and Environmental Engineering
Universitat Politècnica de Catalunya, Barcelona Tech, Spain

Daniel F. Ruiz (daniel.ruiz.restrepo@gmail.com)
Department of Civil and Environmental Engineering
Universitat Politècnica de Catalunya, Barcelona Tech, Spain

Abstract

The paper addresses the numerical simulation of strain localisation in stiff clays that exhibit softening behaviour. An elastoplastic constitutive model developed to incorporate key features of stiff clay behaviour is described first. A non-local formulation is then introduced for the regularisation of the analysis of localisation. A series of analyses were conducted to explore relevant aspects of the numerical simulation of localisation. A 3D analysis was also performed to assess the suitability of the approach presented for 3D applications. Finally, application to the simulation of a laboratory test on Beaucaire marl results in an excellent reproduction of experimental observations.

Keywords: stiff clays, strain localisation, nonlocal plasticity, plane strain.

1. Introduction

Stiff clays usually show a quasi-brittle behaviour under deviatoric loading unless they are subjected to high confining stresses (Gens 2013). They commonly exhibit *strain softening*, which means that, after reaching a maximum, strength decreases as displacements increase until reaching a residual state where the strength no longer decreases even when subject to large displacements (Hvorslev 1937; Lupini et al. 1981; Skempton 1964). The resulting strain field is generally non-homogeneous and deformations tend to localise into thin zones of intense shearing in the form of fractures or slip surfaces (Georgiannou & Burland, 2006; Lenoir *et al*., 2007). This phenomenon is known as *strain localisation*. The numerical simulation of this phenomenon under the framework of continuum mechanics involves a number of difficulties, since it is well-established that standard formulations tend to deliver non-objective results due to the loss of ellipticity of the governing equation at the onset of localisation (Hill, 1962; Mandel, 1966; Thomas, 1961). Particularly, in the simulation of boundary value problems (BVP), this non-objectivity traduces into a strong dependency on the employed mesh (De Borst *et al.*, 1993). Vanishing energy dissipation and localisation into a zone of vanishing volume are obtained as the size of elements is reduced (Bažant & Pijaudier-Cabot, 1988), which is not physically reasonable. Indeed, the actual width of the localised zone in geomaterials seems to be related with their microstructure (Desrues & Viggiani, 2004), providing the material with an internal length scale, missing in the standard continuum formulations. The introduction of an internal length scale can prevent the usual pathologies arising when modelling problems involving localized deformations and different enriched continuum theories have been proposed to introduce such a scale

parameter. Following Bažant & Jirásek (2002), they can be broadly classified into continua with microstructure (e.g. Cosserat & Cosserat, 1909; Eringen, 1966), continua incorporating gradients of strain (gradient theories) (e.g. Mindlin, 1965), and nonlocal models of the integral type (e.g. Eringen, 1981; Pijaudier-Cabot & Bažant, 1987). Other techniques such adaptive mesh refinement (Ortiz & Quigley, 1991; Zienkiewicz & Huang, 1995) or viscoplasticity (Loret & Prevost, 1990; Prevost & Loret, 1990) have also been employed as localisation limiters. All the above-mentioned approaches, sometimes known as *regularisation techniques*, incorporate in some way a length scale to the material behaviour, which tends to control the size of the localised region and prevents the pathological dependency with the employed mesh.

In this paper, the nonlocal integral type approach was applied to a plasticity model, intended for the objective simulation of localised plastic deformations in stiff clays. It incorporates the special weighting function proposed by Galavi & Schweiger (2010), which has shown lower mesh dependency compared with the usual Gaussian function (Summersgill *et al.*, 2017). The model is employed in a series of two-dimensional (2D) plane strain analyses, to explore relevant aspects of the numerical simulation of localisation, such as the thickness of the shear band, its orientation and the onset of localisation in BVPs. A 3D analysis was also performed, in order to assess the suitability of the approach presented for 3D applications. Finally, a real biaxial experiment on Beaucaire marl (Marello, 2004) has been simulated, and the results were compared not only with global measurements but with the entire strain field, observed experimentally using the false relief stereophotogrammetry technique (FRS) (Desrues & Viggiani, 2004).

2. Model formulation

The model described herein represents an enhanced version of the one presented in Mánica *et al.* (2017), for stiff clayey materials. The main enhancement is the ability to simulate objectively the localisation phenomenon by the introduction of the nonlocal approach, which is the main focus of this work. In addition, a different yield function and evolution laws were employed, more consistent with the observed behaviour of stiff clays. However, only a partial version is presented here, where some additional behaviour features of stiff clays, such as stiffness and strength anisotropy, or creep deformations, were not included. The incorporation of these features within the present approach will be addressed in a subsequent paper.

2.1. Local constitutive model

An elastoplastic model is adopted as the basic constitutive law for analysis. Inside the yield surface the response is assumed linear elastic and characterised by Hooke's law. The yield criterion is defined by a hyperbolic approximation of the Mohr-Coulomb envelope (Gens *et al.*, 1990) expressed as,

$$F = \sqrt{\frac{J_2}{f_d(\theta)} + \left(c^* + p_t \tan\phi^*\right)^2} - \left(c^* + p\tan\phi^*\right) \tag{1}$$

where c^* is the asymptotic cohesion, ϕ^* is the asymptotic friction angle, p_t is the isotropic tensile strength, p is mean stress, J_2 is the second invariant of the deviatoric stress tensor $\mathbf{s} = \boldsymbol{\sigma} - p\mathbf{I}$, and θ is Lode's angle. At high mean stresses, Eq. (1) converges to the classical Mohr-Coulomb envelope, and the terms asymptotic cohesion and friction angle refers to this condition. However, at low mean stresses the envelope is curved, with an isotropic tensile strength directly indicated by p_t. This allows us to consider the low

tensile strength usually exhibited by stiff clays, generally overestimated by linear criteria. The shape in the octahedral plane is defined by $f_d(\theta)$, where the following generalised function was employed (van Eekelen, 1980),

$$f_d(\theta) = \alpha\left(1 + B\sin 3\theta\right)^n \qquad (2)$$

where α, B and n are parameters providing a family of surfaces. This can be simplified to a one-parameter function by assuming $n = -0.229$ and $B = 0.85\alpha^{1/2}$, as proposed by van Eekelen (1980). Figure 1 shows the adopted yield function in the $p - J$ and octahedral planes, compared to the classical Mohr-Coulomb criterion. An important limitation is that yielding cannot occur under isotropic compression, a characteristic generally observed in stiff clays (e.g. Burland, 1990). One possibility is to bound the permitted stress space for compressive loading with an additional yielding mechanism, within the framework of multisurface plasticity (e.g. Simo *et al.*, 1988). However, in the present work, only plastic processes under deviatoric loading are of interest, and therefore yielding under isotropic compression was not included in the model.

Isotropic non-linear hardening/softening was considered to reproduce the strength evolution under loading generally observed in stiff clays, which is illustrated in Figure 2 (Jardine *et al.*, 2004). It assumes that the observed initial cohesion is mainly due to the effect of interparticle bonds. At reaching the peak, the breakage of these bonds takes place, and the strength decreases very rapidly, up to a value designated by Burland (1990) as *post-rupture strength*, at which most of the cohesion has been lost. Afterwards, a more gentle reduction takes place, until reaching the residual strength at very large displacements. The remaining cohesion (if any) is completely lost, and the friction angle has reduced considerably. This reduction is generally attributed to a gradual realignment of clay particles on the sliding

surface (Gens 2013). Experimental investigations supporting this conceptual scheme can be found for instance in Calabresi & Manfredini (1973) and Jardine *et al.* (2004). Following this conceptual framework, the evolution laws for the strength parameters are shown in Figure 3, where ε_{eq}^{p} is a scalar state variable defined as,

$$\varepsilon_{eq}^{p} = \left(\boldsymbol{\varepsilon}^{p} : \boldsymbol{\varepsilon}^{p}\right) \tag{3}$$

where $\boldsymbol{\varepsilon}^{p}$ is the plastic strain tensor. The initial position of the yield envelope is given by ϕ_{ini}^{*}, c_{ini}^{*} and $p_{t\,ini}$. It is assumed that plastic deformations before peak strength can occur, so after reaching the yield limit hardening takes place, related to the mobilisation of the apparent friction angle from ϕ_{ini}^{*} to ϕ_{peak}^{*}, according to a hyperbolic function of the equivalent strain. During this hardening phase, the apparent cohesion and tensile strength are assumed to remain constant. The peak strength is reached at χ, i.e. the value of the state variable separating the hardening and softening regimens. Thereafter softening occurs, characterised by an exponential decay function. It has been considered that the rate of softening is not the same for all the strength parameters. A high softening rate is assumed for the apparent cohesion and the tensile strength, related to the degradation and breakage of interparticle bonds. On the other hand, a smaller softening rate is assumed for the apparent friction angle, attributed to a gradual realignment of clay particles that takes the material towards the residual strength. In the residual state, only ϕ_{res}^{*} remains, which in fact becomes a "true" friction angle (ϕ_{res}), since the apparent cohesion and tensile strength have completely disappeared, and a linear criteria (in the $p-J$ plane) is recovered.

As for the development of plastic strains, a non-associated flow rule is adopted. Rather than deriving a specific function for the plastic potential, the flow rule is directly obtained from the yield criterion in the following way,

$$\frac{\partial G}{\partial \boldsymbol{\sigma}} = \omega \frac{\partial F}{\partial p}\frac{\partial p}{\partial \boldsymbol{\sigma}} + \frac{\partial F}{\partial J_2}\frac{\partial J_2}{\partial \boldsymbol{\sigma}} + \frac{\partial F}{\partial \theta}\frac{\partial \theta}{\partial \boldsymbol{\sigma}} \tag{4}$$

where G is the plastic potential and ω is a constant that controls the volumetric component of plastic deformations. With $\omega = 1$ an associated flow rule is recovered, while with $\omega = 0$ no volumetric plastic strains occur. An adequate value for geomaterials should lie between those limits.

2.2. Nonlocal approach

The use of nonlocal models can be traced back to the beginning of the 20th century, although its application as a regularisation technique for numerical simulations did not occur until the 1980s; see Bažant & Jirásek (2002) for a comprehensive review. In a general sense, a nonlocal constitutive model is one where the behaviour at a material point (or at a Gauss point in a finite element simulation) depends not only on its state but also on the state of neighbouring points. This is accomplished by replacing a given variable by its nonlocal counterpart. If $f(\mathbf{x})$ is some local field within a body of volume V, the nonlocal field can be expressed as,

$$\bar{f}(\mathbf{x}) = \int_V w(\mathbf{x},\boldsymbol{\xi})\, f(\boldsymbol{\xi})\, \mathrm{d}\boldsymbol{\xi} \tag{5}$$

where $w(\mathbf{x},\boldsymbol{\xi})$ is a weighting function controlling the importance of neighbouring points as a function of its position ($\boldsymbol{\xi}$), relative to the position of the actual point under consideration

($\mathbf{x}$). Typically, only the distance between them is considered, thus $w(\mathbf{x},\boldsymbol{\xi}) = w_o\left(\|\mathbf{x}-\boldsymbol{\xi}\|\right)$. A Gaussian function has been usually employed (e.g. Bažant & Lin, 1988), where the highest influence occurs at the actual point, and reduces by increasing the distance (Figure 4). The parameter l_s controls the width of the bell-shaped curve, implicitly introducing a length scale to the continuum formulation. Close to the boundaries, averaging should be performed only on the part of the domain that lies within the body. In addition, averaging should not modify a uniform field. Therefore, the weighting function is usually defined in the following normalised form,

$$w(\mathbf{x},\boldsymbol{\xi}) = \frac{w_o\left(\|\mathbf{x}-\boldsymbol{\xi}\|\right)}{\int_V w_o\left(\|\mathbf{x}-\boldsymbol{\zeta}\|\right)\mathrm{d}\boldsymbol{\zeta}} \tag{6}$$

Different nonlocal models are obtained depending on which variable (or variables) is considered nonlocal. For instance, in the case of nonlocal plasticity formulations, different alternatives have been studied, such as elastic strains (Eringen, 1981), total strains (Eringen, 1983), plastic strains or the plastic multiplier (Bažant & Lin, 1988), or the state variable controlling softening (Planas *et al.*, 1993). However, under certain circumstances, these formulations may show undesirable effects such as stress locking, vanishing energy dissipation, or localisation into a zone of vanishing volume (Bažant & Jirásek, 2002). An improved formulation, often called *over-nonlocal*, was proposed by Brinkgreve (1994) where the averaged softening variable is obtained through a linear combination of the local and nonlocal variables,

$$\bar{\kappa}(\mathbf{x}) = (1-\mu)\kappa(\mathbf{x}) + \mu\int_V w(\mathbf{x},\boldsymbol{\xi})\kappa(\boldsymbol{\xi})\mathrm{d}\boldsymbol{\xi} \tag{7}$$

where κ is an arbitrary state variable controlling softening, and μ is a new parameter controlling the relative proportion of the local and nonlocal variables. With $\mu = 0$ the classical local model is recovered, while with $\mu = 1$ the standard nonlocal formulation, described by Eq. (5), is obtained. Although intuition would suggest that an appropriate value should lie between those limits, Brinkgreve (1994) showed that the best results are obtained with $\mu > 1$. The consequence is that the highest influence is removed from of the actual point under consideration and displaced to some distance from it, and in an extreme case, the influence of the actual point can become negative in sign. This approach prevents the localisation of deformations into a zone of vanishing volume. However, the actual size of the localised region will be a combination of l_s and μ, and therefore their selection may be somewhat arbitrary. Following this idea, Galavi & Schweiger (2010) proposed the alternative weighting function depicted in Figure 4. The influence of the actual point is removed and the maximum weight is located at a distance equal to $0.707 l_s$. This function has a similar effect as the over-nonlocal approach, but no additional parameter is required and the size of the localised region is related only to l_s. Summersgill *et al.* (2017) recently compared this latter approach with the standard nonlocal formulation (i.e. Eq. (5) with a Gaussian weighting function) and with the over-nonlocal approach (Brinkgreve, 1994), and concluded that the best results are obtained with the weighting function proposed by Galavi & Schweiger (2010).

In the present research, we applied the approach given by Galavi & Schweiger (2010) to the regularisation of the local model described in Section 2.1. As shown later, and in accordance with the results from Summersgill *et al.* (2017), this approach showed excellent

results in terms of consistency and mesh independence. For the implementation of the stress point algorithm, Eq. (5) and (6) were replaced by the following discrete versions,

$$\bar{\varepsilon}^{\mathrm{p}}_{\mathrm{eq}\,k} = \sum_{l=1}^{N_{\mathrm{G}}} w_{kl}\,\varepsilon^{\mathrm{p}}_{\mathrm{eq}\,l} \tag{8}$$

$$w_{kl} = \frac{w_o\left(\left\|\mathbf{x}_k - \mathbf{x}_l\right\|\right)}{\sum_{m=1}^{N_{\mathrm{G}}}\left(\left\|\mathbf{x}_k - \mathbf{x}_m\right\|\right)} \tag{9}$$

where $\bar{\varepsilon}^{\mathrm{p}}_{\mathrm{eq}}$ is the nonlocal state variable and N_{G} is the total number of Gauss points in the simulation. However, as pointed out by Galavi & Schweiger (2010), the effect of neighbouring points at distances greater than $2l_{\mathrm{s}}$ is quite small (<1.83%), and iteration throughout all Gauss points can be quite inefficient for large BVP. Therefore, only neighbouring points inside an interaction radius of $2l_{\mathrm{s}}$ have been considered for averaging. Since the local model was originally implemented implicitly using the backward Euler method, its nonlocal extension implies that the stress integration cannot be performed in each Gauss point independently, since the resulting state variable in one point will depend (directly or indirectly) on all points regardless of whether they are inside or outside the interaction radius. To overcome this issue, but keeping the algorithm simple and efficient, the iterative technique proposed by Rolshoven (2003) was employed here. The stress integration is performed in each Gauss point independently by assuming that the state variables for all other points are frozen within the current global iteration. Since the actual integration point does not have any influence, nonlocal state variables of all Gauss points can be computed and stored together at the beginning of each global iteration. Furthermore, since Eq. (9) depends only on the relative position of points, it is only computed and stored once at the beginning of the simulation. The nonlocal state variable is computed only for

points in the softening regime. In the hardening regime, before the state variable reaches the value of χ , the model is local.

The developed stress point algorithm incorporates a sub stepping scheme with error control, based on Richardson's (1910) extrapolation, which results in a robust implementation. This algorithm was incorporated as a user defined soil model in the finite element code Plaxis (Brinkgreve *et al.*, 2017), which was used for the simulations described below.

3. Numerical strain localisation analyses

A number of 2D numerical analyses were performed to assess the performance of the developed constitutive model and the non-local formulation in the simulation of localised deformation patterns. They correspond to a drained biaxial plane strain test under displacement control. The analyses do not represent any particular experiment, and the conditions and parameters used in each simulation were simply chosen to evaluate the key aspects of the employed nonlocal approach. Figure 5 shows the size of the analysis domain and the two types of boundary conditions used. In the first type (Figure 5a), fixed horizontal displacements were applied at the top and bottom boundaries to develop a non-homogeneous stress/strain field and favour the onset of localisation. In the second type (Figure 5b), frictionless boundaries are considered with free horizontal displacements at both ends, except for the central node of the bottom boundary in order to avoid an undetermined system. A prescribed downward vertical displacement of 5.0 mm was applied to the top boundary. Table 1 shows the parameters for the base case, while a summary of all performed analyses is presented in Table 2. Table 2 also shows the parameters and/or boundary conditions that have been changed in each analysis with respect to the base case.

The following features of the localisation analyses are now examined: mesh independence, shear band thickness and softening scaling, effect of boundary conditions and imperfections, onset of localisation and shear band orientation.

3.1. Mesh independence

As previously mentioned, analyses involving localised deformations exhibit a marked dependency with the finite element mesh employed. This pathology is demonstrated in the set of analyses A, where six different meshes with increasing number of elements where used. The first type of boundary conditions (Figure 5a) was prescribed. The finite elements were 15-noded triangular with fourth-order interpolation and 12 integration points. In this set of analyses, the local version of the model was employed, i.e. without the nonlocal extension described in section 2.2. Figure 6 shows contour plots of the computed shear strain, defined, in this plane strain condition, as,

$$\varepsilon_s = \left(\varepsilon_1 - \varepsilon_3\right)/2 \tag{10}$$

where ε_1 and ε_3 are the major and minor principal strains. ε_s is a very convenient way to observe the configuration of the localised deformation pattern. The employed meshes are also depicted in the figure. Because of the fixed horizontal displacements at the boundary, stresses concentrate in the four corners of the model, allowing the simultaneous formation of two X-shaped shear bands. However, in analyses A01 and A02, the large size of elements and its orientation interfere with the free propagation of shear bands, resulting in one of them developing more than the other one. In the remaining analyses, elements are small enough to avoid this interference and therefore both bands are symmetrical to each other. In any case, the mesh dependency can be clearly recognized by the decreasing

thickness of shear bands when increasing the number of elements (and therefore decreasing its size). After the onset of localisation, Gauss points outside the band unload elastically, and plastic processes concentrate within it. Therefore, a decreasing thickness of the band translates to a decreasing amount of dissipated energy. At the limit, with elements size tending to zero, the dissipation will also tend to zero, which is not physically reasonable. This decreasing dissipation is apparent in Figure 7 that shows the vertical deviator load (per meter thickness) against the prescribed vertical displacement. A more brittle response is obtained when the number of elements is increased.

In the B set of analyses, the nonlocal extension of the model was employed, with an internal length scale of 1.0 cm. The nonlocal approach requires a minimum amount of Gauss points inside the interaction radius to compute the nonlocal variable. For the same kind of elements, as the ones employed here, Galavi & Schweiger (2010) suggested that the following condition must be fulfilled,

$$l_s \geq L_{el} \tag{11}$$

where L_{el} is the maximum length of an element in the FE mesh. For this reason, meshes with 16, 63 and 167 elements were discarded for this set of analyses. Figure 8 shows the obtained contour plots of shear strain. Unlike set A, the same localisation pattern and the same shear band thickness were obtained in all analyses regardless the number of elements. Dissipated energy is now also mesh-independent, and therefore a practically unique load-displacement curve was obtained in all three analyses (Figure 9).

3.2. Shear band thickness and softening scaling

The effect of l_s was explored in the set C, where the case B03 was analysed for different values of l_s. Figure 10 shows the computed contours of shear strain. As l_s decreases, the interaction radius also decreases, and therefore plastic deformations tend to localise in a narrower zone. Table 3 shows the shear band thickness from these analyses. The boundary of the shear zone is defined as the location where a sudden jump in the field of incremental displacements take place. The numerical shear band thickness is roughly equal to the length scale parameter, as already observed by Galavi & Schweiger (2010). Nevertheless, since the constitutive behaviour is the same in all analyses (the same local model, with the same parameters), a thinner shear band entails a lower energy dissipation, and therefore a more brittle response (Figure 11). Consequently, for a given load-displacement curve, there exists a relationship between the length scale parameter and the softening rate.

To properly apply the nonlocal approach in the simulation of a given material, l_s should be chosen to obtain a shear band thickness similar than those observed experimentally. Then, the softening rate can be adjusted to match a given load-displacement curve. However, localisation processes in stiff clays tend to be more discrete, in the form of fractures or slip surfaces (Georgiannou & Burland, 2006; Lenoir *et al.*, 2007), surrounded by a small zone of intense shearing of a few micrometres (Laurich *et al.*, 2014). Since a number of Gauss points inside the interaction radius are required to compute the nonlocal variable, it appears unfeasible to apply the nonlocal approach for stiff clays as it would require an excessively refined mesh. However, this can be overcome by assuming that the effects of the actual fracture and sheared zone can be merged into a numerical shear band of larger size. In this case, the mesh should be as refined as possible, but without exceeding available computational capacities. The length scale parameter should be chosen according to Eq.

(11), which will result in the smallest allowable band thickness for a given mesh refinement. Then, the desired macroscopic material behaviour (e.g. a given load-displacement curve) can be reproduced by adjusting the softening rate of the model. Therefore, the post-localisation behaviour of the simulation will be the result of the combination of both, the length scale parameter and the softening rate. This technique is known as *softening scaling*, first suggested by Pietruszczak & Mroz (1981), and later applied by others (Brinkgreve, 1994; Galavi & Schweiger, 2010; Marcher, 2003; Schädlich, 2012), which allows us to merge the effects of the real fracture process zone into a larger numerical shear band, in accordance with a reasonable amount of computational resources. This is of paramount importance when dealing with real engineering situations.

In the constitutive model described here the total softening rate is defined by parameters b_c and b_ϕ, controlling the rate of reduction of cohesion (and tensile strength) and friction angle respectively. Thus, in principle, both parameters should be adjusted when defining the target softening rate. Nevertheless, as previously stated, the friction angle reduction in stiff clays soils is generally slow, and requires large deformations. When dealing with small softening rates, the usual pathologies arising from the continuum simulation of strain localisation may become unimportant (Pietruszczak & Mroz, 1981). This is clearly demonstrated in Figure 12, where different meshes were analysed using the local version of the model, but with b_c set equal to zero, i.e. just considering a gentle reduction of the friction angle. Despite having used different sizes of elements, the response is not mesh-dependent, and a unique load-displacement curve was obtained from all analyses. Therefore, since the small rate of reduction of the friction angle does not result in mesh

dependent results, the adjustment of the softening rate, for a given l_s, can be performed only through variation of b_c.

Assuming, for example, that the load-displacement curve from the analysis B03 is the desired macroscopic behaviour, the analyses from set C were again performed (set E), but with a softening rate adjusted to retrieve the desired response. Figure 13 shows how a unique load-displacement curve can be obtained from the different analyses by using in each of them an appropriate value of b_c. The relationship obtained between the softening rate and the length scale parameter is depicted in Figure 14. Despite using an exponential softening law, the softening rate seems to scale linearly with l_s, as already suggested by others (Galavi & Schweiger, 2010; Marcher, 2003; Schädlich, 2012).

3.3. Effect of boundary conditions and imperfections

The overall behaviour of problems exhibiting localisation does not only depend on the constitutive behaviour, but boundary conditions have a profound influence on the obtained configuration of the localised deformation pattern. This is clearly shown by the analysis F01, where frictionless ends were used (Figure 5b). Naturally, these conditions lead to a homogeneous stress/strain field, where localisation cannot take place. Therefore, a geometric imperfection was introduced to enforce localisation; the top boundary was shifted to the right 0.5 mm with respect to the bottom one. Upon loading, this imperfection causes a nonhomogeneous stress/strain distribution, where plastic deformations first accumulate at the top-left and bottom-right corners. Therefore, unlike previous analyses where two X-shaped shear bands formed simultaneously, only a single shear band is generated across the sample, joining these two corners (Figure 15a).

Another commonly employed method to induce the onset of localisation is to incorporate a weak element, from which the shear band can propagate. This was done in analysis F02 where the weak element was located at the top-right corner and had a cohesion of 100 kPa, i.e. half than the rest of elements. No geometrical imperfections are introduced in this analysis. A single shear band is also generated (Figure 15b), but since it initiates in the top-right corner, it has the opposite orientation with respect to the analysis F01.

3.4. Onset of localisation

Strain localisation is a progressive process and the definition of an onset is difficult. Non-uniform strain fields can appear at very early stages of the deformation but experimental evidence suggests that the onset of a persistent shear band often occurs near the global peak strength or slightly before (Desrues & Viggiani, 2004). In the context of plasticity theory, the localised failure condition at the constitutive level has been related to the singularity of the so-called acoustic or localisation tensor (Hill, 1962; Ortiz, 1987; Rice, 1976), i.e. when the following condition is met:

$$\det\left(\mathbf{Q}\right) = \det\left(\mathbf{n}\cdot\mathbf{D}\cdot\mathbf{n}\right) = 0 \tag{12}$$

where $\mathbf{Q}$ is the acoustic tensor, $\mathbf{D}$ is the tangent stiffness matrix and $\mathbf{n}$ is the normal to the discontinuity surface. However, instability of a single Gauss point (or a number of them) does not necessarily imply a global instability of the BVP.

In the present study, the onset of localisation at a global level was objectively identified by the evolution of the second derivative of the shear strain with respect to time, averaged for all Gauss points:

$$\bar{\varepsilon}_s'' = \frac{1}{N_G}\sum_{i=1}^{N_G}\frac{d^2\varepsilon_s}{dt^2}_i \quad (13)$$

where t is the simulation time. It can be viewed as some sort of global shear strain acceleration. Figure 16 shows the evolution of this variable during analysis E03. At the beginning the response is purely elastic, a linear relationship exists between the applied constant displacement rate and the shear strain rate and, therefore, $\bar{\varepsilon}_s''$ is equal to zero. Due to the fixed horizontal displacements boundary condition, hardening is initially attained at Gauss points close to the corners of the model. As plastic hardening takes place, the rate of accumulation of shear strains slowly increases, as reflected in a gentle increase of $\bar{\varepsilon}_s''$. Subsequently softening is also initially attained at Gauss points close to the corners. From this point on, the increase of $\bar{\varepsilon}_s''$ accelerates. Nevertheless, the remaining points, still in the hardening regime, contribute to the global stability of the model. When a sufficient number of Gauss points enter the softening regime (1909 in this case), plastic shear strains suddenly increase along what will be the shear bands, causing a jump in $\bar{\varepsilon}_s''$. This point is taken here as the onset of localisation of the BVP (Figure 16). From this point on, $\bar{\varepsilon}_s''$ does not show a smooth evolution and exhibits oscillations during the rest of the simulation. It is interesting to notice that this instability point does not necessarily take place at the peak strength, and in this case occurs slightly before it, as experimental evidence often indicates (Desrues & Viggiani, 2004).

3.5. Shear band orientation

The orientation of shear bands in geomaterials (or at least in granular ones) has been historically bounded by two limits. The upper bound is given by Coulomb's theory, in

which shear band orientation coincides with the inclination of the plane where the maximum ratio of shear to normal stress occurs:

$$\theta_C = 45^o + \frac{\phi}{2} \tag{14}$$

where θ_C is Coulomb's angle and ϕ is the friction angle. The lower bound is given by Roscoe's (1970) criterion where the orientation is determined by the zero extension direction with respect to the axis of minimum principal strain rate, leading to,

$$\theta_R = 45^o + \frac{\psi}{2} \tag{15}$$

where θ_R is Roscoe's angle and ψ is the dilation angle. Most laboratory observations of shear banding fall within these limits (e.g. Alshibli & Sture, 2000; Arthur *et al.*, 1977; Desrues & Viggiani, 2004; Finno *et al.*, 1997; Vermeer, 1990). Vermeer (1990) also suggested that a given material tends to one of them depending on the particle size; coarse sands tend towards Roscoe's orientation, whereas fine sands tend to show Coulomb's orientation. However, Desrues & Viggiani (2004) argued that the orientation of a shear band is not directly related to the particles size. They also pointed out that the orientation is not constant and may evolve throughout a test. An intermediate relationship between Coulomb's and Roscoe's solutions was also proposed by Arthur *et al.* (1977) (Eq. (*16*)) and later supported by Vardoulakis (1980) through a bifurcation analysis.

$$\theta_A = 45^o + \frac{\phi + \psi}{4} \tag{16}$$

where θ_A is Arthur's angle.

In Figure 17, the resulting shear band orientation from analysis E03 was compared to those obtained from Eq. (14) - (16). The friction and dilation angles for the present plane strain

condition were computed throughout the simulation at a Gauss point inside the shear band (its location is also shown in Figure 17), according to:

$$\phi = \arcsin\left[\frac{(\sigma_1/\sigma_3)-1}{(\sigma_1/\sigma_3)+1}\right] \tag{17}$$

$$\psi = \arcsin\left[-\frac{(\mathrm{d}\varepsilon_1/\mathrm{d}\varepsilon_3)+1}{(\mathrm{d}\varepsilon_1/\mathrm{d}\varepsilon_3)-1}\right] \tag{18}$$

where σ_1 and σ_3 are the major and minor principal stresses and $\mathrm{d}\varepsilon_1$ and $\mathrm{d}\varepsilon_3$ are the major and minor principal strain increments. The vertical displacement at the peak of the global load-displacement curve is indicated in the figure, along with the value corresponding to the onset of localisation of the BVP. Coulomb's and Arthur's orientations seem to overestimate the obtained shear band inclination of 55º, which appears to coincide with Roscoe's criterion computed at the onset of localisation.

In Figure 18 Roscoe's orientation was also compared with the shear bands from analyses of set F, where smooth boundary conditions were employed. Here, the geometrical imperfection and weak element in analyses F01 and F02, respectively used to favour the onset of localisation, did not produce large heterogeneities compared to models with rough boundaries. Fewer points have begun softening before the peak of the load-displacement curve, and their number is insufficient to produce the instability of the BVP. As a result, the onset of localisation coincides with the global peak strength in both analyses. Despite having used the same parameters than in E03, each analysis delivered a different shear band orientation. Nevertheless, both of them coincide with Roscoe's orientation at the onset of localisation.

Since the amount of dilation at the onset of localisation seems to control the orientation of the shear band, a given BVP should yield a different orientation if the flow rule (Eq. (*4*)) of

the constitutive law is modified. The latter was demonstrated in the analyses of set G. They share the same characteristics with the analysis E03, but different values of ω were employed, controlling the amount of plastic volumetric strains during loading. Figure 19 shows the shear bands obtained in terms of shear strains contours. As ω is reduced, a lower dilation angle operates at the onset of localisation, producing a gentler inclination of the shear bands. Figure 20 compares the obtained inclinations to those computed from Eq. (15). Here the vertical displacements were normalised with the corresponding value at the onset of localisation. Again, the obtained orientations at the onset of localisation are consistent with Roscoe's criterion.

The orientation of the numerical shear bands is not in fact constant throughout the simulations; a slight change has been observed in all analyses. For example, in analysis E03 the shear band orientation reduces by about 0.3^{o} from the instant it is first identified, until the end of the simulation. Certainly, this change is small and does not alter the conclusions drawn before, but it suggests that once a persistent shear band has formed, its orientation may still evolve due to changes in the direction of plastic flow, that in this case occurs due to a small reduction of the friction angle during softening (see Eq. (*1*) and (*4*) and Figure 3). To verify this hypothesis, a severe modification in the flow rule was enforced in analysis H01, by considering that ω is no longer constant but it evolves during the simulation according to,

$$\omega = \begin{cases} 1 & \left(\varepsilon_{eq}^{p} \le \chi\right) \\ e^{-b_{\omega}\varepsilon_{eq}^{p}} & \left(\varepsilon_{eq}^{p} > \chi\right) \end{cases} \tag{19}$$

where b_{ω} is a parameter controlling the rate of reduction of ω and takes a value equal to 20 in this analysis. Apart from this difference, analysis H01 share the same characteristics as

analysis E03. Figure 21 shows the evolution of the shear band orientation throughout the simulation compared to that derived from Eq. (15). The drastic change in the direction of plastic flow during the simulation is evidenced by a reduction over 23º in the dilation angle from its maximum value, which in turn leads to a reduction of 11.9º in the predicted shear band orientation. Unlike previous analyses, a noticeable reduction of the shear band inclination was identified here of around three degrees. However, this reduction is much smaller than that predicted due to changes in the dilation angle. These results suggest that once a persistent shear band has formed, it is difficult to modify its orientation, and it is only possible through important changes in the direction of plastic flow.

4. 3D modelling of localisation

The plane strain cases analysed in this study offer a good opportunity to assess the nonlocal approach in a 3D simulation. A 2D plane strain analysis is, in fact, a representation of a 3D problem with infinite extent in the perpendicular direction. Therefore, a 3D simulation with a finite extent in this direction, but with appropriate boundary conditions representing the infinite extent, should give in principle the same results as the 2D model. This was verified by analysis I01, which is a 3D version of the analyses of group B. Figure 22a shows the model geometry and boundary conditions, which are analogous to those depicted in Figure 5a, but with a thickness of three centimetres. The null displacements in the "y" direction at the front and back faces ensure plane strain condition. The employed mesh is also shown in the same figure. It comprises 6680 tetrahedral 10-noded finite elements with second-order interpolation and four integration points. The condition given by Eq. (11) is also fulfilled here, but L_{el} is interpreted as the larger edge of the tetrahedra.

Figure 22b shows the computed field of shear strain. By comparing it with Figure 8, it can be noted that the same localisation pattern and the same width of the shear bands were obtained with the 3D model. The difference is that now the localised zone has an additional dimension, i.e. it is a 3D region where plastic deformations accumulate. Figure 23 shows the load-displacement curve compared to those of set B. Notice that the scale of the vertical axis is now kN, so the curves from the group B were adjusted accordingly. Again, the 3D model yielded almost exactly the same curve than the 2D model. These results provide confidence in the application of the employed approach for the simulation of 3D problems involving localised deformations.

5. Plane strain tests in Beaucaire marl

A real plane strain experiment on Beaucaire marl reported by Marello (2004) was also simulated to demonstrate the capability of the developed constitutive model to simulate localised deformations in stiff clays. The Beaucaire marl is a sedimentary overconsolidated clayey material deposited during Pleistocene, lying in the transition zone between hard soils and weak rocks. Some reference properties are summarised in Table 4. In particular, attention is focused on test MBLL16 that is part of a large experimental program to investigate the phenomenon of shear banding in saturated stiff clayey soils (Marello, 2004; Marello *et al.*, 2004; Viggiani & Desrues, 2004). Figure 24 shows the dimensions of the sample and a diagram of the employed plane strain compression apparatus at the laboratory 3S of Grenoble. The glass plates allow taking photographs of the in-plane deformation of the sample throughout the experiment, from which the strain fields can be later determined. For the experiment considered (MBLL16), FRS was employed to derive the deformation

fields. A detailed description of this technique and of the apparatus can be found in Desrues & Viggiani (2004).

After backpressure saturation and swelling under the confinement pressure, an approximately isotropic initial stress condition of 313 kPa was attained in the specimen. Shearing was performed under displacement control, at a rate of 0.004 mm/min and under globally drained conditions. Figure 25 shows a picture of the specimen after the test, where the localised nature of deformations can be readily identified. Two roughly symmetrical shear bands formed at the bottom of the sample, from a point where a weak spot is believed to exist. Details on the testing procedures and results are given in Marello (2004).

Figure 26a shows the geometry, mesh and boundary conditions of the 2D model used for the simulation of the experiment. As silicon grease was employed to lubricate surfaces in contact with the specimen, smooth boundaries were considered for the upper and lower ends. The node with fixed horizontal displacements, employed to prevent an undetermined system, was placed in the upper boundary. Since the formation of the shear bands begins at the lower boundary (Figure 25), the placement of the fixed node there would have interfered with their propagation. As the test was performed under globally drained conditions and with a low displacement rate, hydromechanical coupling was not considered here and only a mechanical simulation was performed. The parameters adopted are listed in Table 5. A random variation (±5%) of the apparent cohesion was also introduced to generate a non-uniform deformation field and facilitate the formation and propagation of the shear bands (Figure 26b). In addition, a single weak element with null asymptotic cohesion was included, the location is depicted in Figure 26b. This element represents a weak spot in the material, from which the shear bands propagate.

Figure 27 shows the deviator load vs. the global axial strain (i.e. computed from the vertical displacement of the loading platen and the initial height of the sample) derived from the experiment, together with the simulation results. A good agreement between both is clearly apparent. The open crosses designate the points where photographs were taken during the test to obtain the deformation fields. Figure 28a shows the incremental shear strain field between points 5 and 6, where the persistent localisation pattern was clearly visible. The two persistent shear bands were well captured by the FRS technique (compare with Figure 25). Figure 28b and Figure 28c shows the incremental shear strain field obtained from the simulation in the same interval. In Figure 28b results are presented in the same format than Marello (2004) to allow direct comparison between them. Note that the scale is also the same. The simulation satisfactorily captured the localised deformation pattern observed in the experiment. In addition, similar values of shear strain were obtained. The point where the shear bands initiate was determined by the location of the weak element. However, no assumptions were made regarding the orientation of the shear bands, which is the result of the constitutive behaviour. The thickness of the shear bands is also quite similar although both, the FRS and the simulation, overestimate the real width of the localised zone (see Figure 25). The first one due to the coarseness of the grid where the displacement field was computed and the second one is the result of the chosen length scale parameter. Nevertheless, these larger numerical shear bands represent adequately the real deformation process, and therefore a good agreement with the global response was obtained.

6. Conclusions

A nonlocal approach was applied to an elastoplastic constitutive model for the objective simulation of localised deformations in stiff clays. A number of analyses were performed, from which the following conclusion can be drawn:

- The combination of the constitutive model with the nonlocal approach using the averaging function from Galavi & Schweiger (2010) provides excellent results preventing the usual pathologies arising from the continuum simulation of strain localisation. Shear band thickness and global load-displacement curves are independent of mesh refinement and element size.
- Softening scaling is required in the analysis of real problems because of the very small thickness of localised strains in still clayey materials. It has been found that, in spite of the nonlinearity of the behaviour modelled, the relationship between the length scale parameter and the softening rate seems to be linear.
- The overall behaviour of problems exhibiting localisation does not only depend on the constitutive behaviour, boundary conditions and the presence of imperfections have a significant influence on the computed configuration of the localised deformation pattern.
- A criterion is proposed to identify objectively the onset of localisation in a BVP. It was observed that this onset occurs either at the peak strength, or slightly before it. This is consistent with experimental evidence (Desrues & Viggiani, 2004).
- The orientation of the numerical shear bands at the point identified as the onset of localisation seems to coincide with Roscoe's criterion based on the orientation of the zero-extension line. It has also been observed that, once a persistent shear band has

formed, it is difficult to modify its orientation. Modest orientation changes are only possible through drastic changes in the direction of plastic flow.

- The formulation developed has proved to be readily transferable to 3D computations.
- The satisfactory simulation of a real biaxial experiment provides additional confidence in the application of the presented approach for the simulation of localised deformation in stiff clays.

Acknowledgements

The financial and technical assistance of ANDRA to the work presented is gratefully acknowledged. The first author has been supported by a Conacyt scholarship (Reg. No. 270190).

References

Alshibli, K. A., and Sture, S. (2000). "Shear band formation in plane strain experiments of sand." *Journal of Geotechnical and Geoenvironmental Engineering*, 126(6), 495–503.

Arthur, J. R. F., Dunstan, T., Al-Ani, Q. A. J. L., and Assadi, A. (1977). "Plastic deformation and failure in granular media." *Géotechnique*, 27(1), 53–74.

Bažant, Z. P., and Jirásek, M. (2002). "Nonlocal integral formulations of plasticity and damage: survey of progress." *Journal of Engineering Mechanics*, 128(11), 1119–1149.

Bažant, Z. P., and Lin, F.-B. (1988). "Nonlocal yield limit degradation." *International Journal for Numerical Methods in Engineering*, 26(8), 1805–1823.

Bažant, Z. P., and Pijaudier-Cabot, G. (1988). "Nonlocal continuum damage, localization instability and convergence." *Journal of Applied Mechanics*, 55(2), 287–293.

De Borst, R., Sluys, L. J., Mühlhaus, H.-B., and Pamin, J. (1993). "Fundamental issues in finite element analyses of localization of deformation." *Engineering Computations*, 10(2), 99–121.

Brinkgreve, R. B. J. (1994). "Geomaterials models and numerical analysis of softening."

Delft University of Technology.

Brinkgreve, R. B. J., Kumarswamy, S., and Swolfs, W. M. (2017). *PLAXIS 2D 2017*. Plaxis bv, Delft, Netherlands.

Burland, J. B. (1990). "On the compressibility and shear strength of natural clays." *Géotechnique*, 40(3), 329–378.

Calabresi, G., and Manfredini, G. (1973). "Shear strength characteristics of the jointed clay of S. Barbara." *Géotechnique*, 23(2), 233–244.

Cosserat, E., and Cosserat, F. (1909). *Théorie des corps déformables*. Librairie Scientifique A. Hermann et Fils, Paris.

Desrues, J., and Viggiani, G. (2004). "Strain localization in sand: an overview of the experimental results obtained in Grenoble using stereophotogrammetry." *International Journal for Numerical and Analytical Methods in Geomechanics*, 28(4), 279–321.

van Eekelen, H. A. M. (1980). "Isotropic yield surfaces in three dimensions for use in soil mechanics." *International Journal for Numerical and Analytical Methods in Geomechanics*, 4(1), 89–101.

Eringen, A. C. (1966). "Mechanics of micromorphic materials." *11th Int. Congr. of Applied Mechanics*, Springer, Berlin, 131–138.

Eringen, A. C. (1981). "On nonlocal plasticity." *International Journal of Engineering Science*, 19(12), 1461–1474.

Eringen, A. C. (1983). "Theories of nonlocal plasticity." *International Journal of Engineering Science*, 21(7), 741–751.

Finno, R. J., Harris, W. W., Mooney, M. A., and Viggiani, G. (1997). "Shear bands in plane strain compression of loose sand." *Géotechnique*, 47(1), 149–165.

Galavi, V., and Schweiger, H. F. (2010). "Nonlocal multilaminate model for strain softening analysis." *International Journal of Geomechanics*, 10(1), 30–44.

Gens, A. (2013). "On the hydromechanical behaviour of argillaceous hard soils-weak rocks." *Proceedings of the 15th European Conference on Soil Mechanics and Geotechnical Engineering - Geotechnics of Hard Soils - Weak Rocks*, A. Anagnostopoulos, M. Pachakis, and C. Tsatsanifos, eds., IOS Press, 71–118.

Gens, A., Carol, I., and Alonso, E. E. (1990). "A constitutive model for rock joints formulation and numerical implementation." *Computers and Geotechnics*, 9(1–2), 3–

20.

Georgiannou, V. N., and Burland, J. B. (2006). “A laboratory study of slip surface formation in an intact natural stiff clay.” *Géotechnique*, 56(8), 551–559.

Hill, R. (1962). “Acceleration waves in solids.” *Journal of the Mechanics and Physics of Solids*, 10(1), 1–16.

Hvorslev, M. (1937). *Über die Festigkeitseigenschaften gestörter bindiger Böden*. København Gad.

Jardine, R. J., Gens, A., Hight, D. W., and Coop, M. R. (2004). “Developments in understanding soil behaviour.” *Advances in geotechnical engineering: The Skempton conference*, Thomas Telford, London, 103–206.

Laurich, B., Urai, J. L., Desbois, G., Vollmer, C., and Nussbaum, C. (2014). “Microstructural evolution of an incipient fault zone in Opalinus Clay: Insights from an optical and electron microscopic study of ion-beam polished samples from the Main Fault in the Mt-Terri Underground Research Laboratory.” *Journal of Structural Geology*, 67, 107–128.

Lenoir, N., Bornert, M., Desrues, J., Bésuelle, P., and Viggiani, G. (2007). “Volumetric digital image correlation applied to x-ray microtomography images from triaxial compression tests on argillaceous rock.” *Strain*, 43(3), 193–205.

Loret, B., and Prevost, J. H. (1990). “Dynamic strain localization in elasto-(visco-)plastic solids, Part 1. General formulation and one-dimensional examples.” *Computer Methods in Applied Mechanics and Engineering*, 83(3), 247–273.

Lupini, J. F., Skinner, A. E., and Vaughan, P. R. (1981). “The drained residual strength of cohesive soils.” *Géotechnique*, 31(2), 181–213.

Mandel, J. (1966). “Conditions de stabilité et postulat de drucker.” *Rheology and Soil Mechanics / Rhéologie et Mécanique des Sols*, J. Kravtchenko and P. M. Sirieys, eds., Springer Berlin Heidelberg, 58–68.

Mánica, M., Gens, A., Vaunat, J., and Ruiz, D. F. (2017). “A time-dependent anisotropic model for argillaceous rocks. Application to an underground excavation in Callovo-Oxfordian claystone.” *Computers and Geotechnics*, 85, 341–350.

Marcher, T. (2003). “Nichtlokale Modellierung der Entfestigung dichter Sande und steifer Tone.” University of Stuttgart.

Marello, S. (2004). “Studio del comportamento meccanico di argille consistenti e marne (Etude du comportement mécanique des argiles raides et des marnes).” Politecnico di Torino (Italy), Université J. Fourier de Grenoble (France).

Marello, S., Lenoir, N., Viggiani, G., Bésuelle, P., Desrues, J., and Di Michiel, M. (2004). “Shear banding in plane strain compression of Beaucaire Marl studied through post-mortem X-ray micro tomography.” *X-ray CT for Geomaterials; Soils, Concrete, Rocks*, J. Otani and Y. Obara, eds., A.A. Balkema, 139–146.

Mindlin, R. D. (1965). “Second gradient of strain and surface tension in linear elasticity.” *International Journal of Solids and Structures*, 1(4), 417–438.

Ortiz, M. (1987). “An analytical study of the localized failure modes of concrete.” *Mechanics of Materials*, 6, 159–174.

Ortiz, M., and Quigley, J. J. (1991). “Adaptive mesh refinement in strain localization problems.” *Computer Methods in Applied Mechanics and Engineering*, 90(1–3), 781–804.

Pietruszczak, S., and Mroz, Z. (1981). “Finite element analysis of deformation of strain-softening materials.” *International Journal for Numerical Methods in Engineering*, 17(3), 327–334.

Pijaudier-Cabot, G., and Bažant, Z. P. (1987). “Nonlocal Damage Theory.” *Journal of Engineering Mechanics*, 113(10), 1512–1533.

Planas, J., Elices, M., and Guinea, G. V. (1993). “Cohesive cracks versus nonlocal models: closing the gap.” *International Journal of Fracture*, 63(2), 173–187.

Prevost, J. H., and Loret, B. (1990). “Dynamic strain localization in elasto-(visco-)plastic solids, part 2. plane strain examples.” *Computer Methods in Applied Mechanics and Engineering*, 83(3), 275–294.

Rice, J. R. (1976). “The localization of plastic deformation.” *Proceedings of the 14th intenational congress on theoretical and applied mechanics*, W. T. Koiter, ed., North-Holland Publishing Co., Delft, 207–220.

Richardson, L. F. (1910). “The approximate arithmetical solution by finite differences of physical problems involving differential equations, with an application to the stresses in a masonry dam.” *Philosophical Transactions of the Royal Society A*, 210(459–470), 307–357.

Rolshoven, S. (2003). “Nonlocal plasticity models for localized failure.” École Polytechnique Fédérale de Lausanne.

Roscoe, K. H. (1970). “The influence of strains in soil mechanics.” *Géotechnique*, 20(2), 129–170.

Schädlich, B. (2012). “A multilaminate constitutive model for stiff soils.” Technische Universität Graz.

Simo, J. C., Kennedy, J. G., and Govindjee, S. (1988). “Non-smooth multisurface plasticity and viscoplasticity. Loading/unloading conditions and numerical algorithms.” *International Journal for Numerical Methods in Engineering*, 26(10), 2161–2185.

Skempton, A. W. (1964). “Long-term stability of clay slopes.” *Geotechnique*, 14(2), 77–102.

Summersgill, F. C., Kontoe, S., and Potts, D. M. (2017). “Critical assessment of nonlocal strain-softening methods in biaxial compression.” *International Journal of Geomechanics*, 17(7), 1–14.

Thomas, T. Y. (1961). *Plastic flow and fracture in solids*. Academic Press.

Vardoulakis, I. (1980). “Shear band inclination and shear modulus of sand in biaxial tests.” *International Journal for Numerical and Analytical Methods in Geomechanics*, 4(2), 103–119.

Vermeer, P. A. (1990). “The orientation of shear bands in biaxial tests.” *Géotechnique*, 40(2), 223–236.

Viggiani, G., and Desrues, J. (2004). “Experimental observation of shear banding in stiff clay.” *Geotechnical Innovations*, R. B. J. Brinkgreve, ed., Verlag Glückauf Essen, 649–658.

Zienkiewicz, O. C., and Huang, M. (1995). “Localization problems in plasticity using finite elements with adaptive remeshing.” *International Journal for Numerical and Analytical Methods in Geomechanics*, 19(2), 127–148.

Figures’ caption

Figure 1. Yield criterion in the a) p-J and b) octahedral planes

Figure 2. Conceptual scheme for the strength of stiff plastic clays (Jardine *et al.*, 2004)

Figure 3. Hardening/softening rules

Figure 28. Incremental field of shear strain from a plane strain compression test on stiff Beaucaire marl: (a) experimental (Marello, 2004) and (b,c) simulation results

Tables' caption

Table 1. Parameters of base case analysis A01

Table 2. Analyses performed

Table 3. Obtained shear band thickness from the set of analysis C

Table 4. Reference properties of the Beaucaire marl (from Marello *et al.*, 2004)

Table 5. Parameters for the simulation of the test on Beaucaire marl

Tables

Table 1. Parameters of base case analysis A01

Parameter	Symbol	Units	Value
Young's modulus	E	[kPa]	20000
Poisson's ratio	ν	[-]	0.2
Initial asymptotic friction angle	ϕ^*_{ini}	[º]	10
Peak asymptotic friction angle	ϕ^*_{peak}	[º]	20
Residual friction angle	ϕ^*_{res}	[º]	15
Asymptotic cohesion	c^*_{ini}	[kPa]	200
Tensile strength	$p_{\text{t ini}}$	[kPa]	0
Equivalent strain at peak strength	χ	[-]	0.01
Constant in hardening law	a_ϕ	[-]	0.001
Rate of reduction of friction angle	b_ϕ	[-]	2
Rate of reduction of cohesion	b_c	[-]	10
Non-associative constant	ω	[-]	1
Length scale parameter	l_s	[cm]	n/a

Table 2. Analyses performed

Analysis	Boundary conditions	No. elements	Variation with respect to A01
A01	Rough	16	-
A02	Rough	63	-
A03	Rough	167	-
A04	Rough	343	-
A05	Rough	789	-
A06	Rough	1303	-
B01	Rough	343	l_s = 1.0 cm
B02	Rough	789	l_s = 1.0 cm
B03	Rough	1303	l_s = 1.0 cm
C01	Rough	1303	l_s = 0.8 cm
C02	Rough	1303	l_s = 0.6 cm
C03	Rough	1303	l_s = 0.4 cm
D01	Rough	343	b_c = 0
D02	Rough	789	b_c = 0
D03	Rough	1303	b_c = 0
E01	Rough	1303	l_s = 0.8 cm, b_c = 8.6
E02	Rough	1303	l_s = 0.6 cm, b_c = 7.0
E03	Rough	1303	l_s = 0.4 cm, b_c = 5.2
F01	Smooth	1303	l_s = 0.4 cm, b_c = 5.2, geometrical imperfection
F02	Smooth	1303	l_s = 0.4 cm, b_c = 5.2, weak element
G01	Rough	1303	l_s = 0.4 cm, b_c = 5.2, ω = 0.8
G02	Rough	1303	l_s = 0.4 cm, b_c = 5.2, ω = 0.6
G03	Rough	1303	l_s = 0.4 cm, b_c = 5.2, ω = 0.4
G04	Rough	1303	l_s = 0.4 cm, b_c = 5.2, ω = 0.2
G05	Rough	1303	l_s = 0.4 cm, b_c = 5.2, ω = 0.0
H01	Rough	1303	l_s = 0.4 cm, b_c = 5.2, b_ω = 20
I01	Rough	6680	l_s = 1.0 cm, 3D

Table 3. Obtained shear band thickness from the set of analysis C

Analysis	l_s [cm]	Shear band thickness [cm]
B03	1.00	0.95
C01	0.80	0.77
C02	0.60	0.58
C03	0.40	0.44

Table 4. Reference properties of the Beaucaire marl (from Marello *et al.*, 2004)

Clay content [%]	30
Calcium carbonate content [%]	up to 30
Water content [%]	23 – 25
Liquid limit [%]	40 – 45
Plastic index [%]	21 – 25
Vertical yield stress, $\sigma_y^{'}$ [kPa]	2000
Uniaxial compressive strength, UCS [kPa]	900

Table 5. Parameters for the simulation of the test on Beaucaire marl

Parameter	Symbol	Units	Value
Young's modulus	E	[kPa]	36000
Poisson's ratio	ν	[-]	0.37
Initial asymptotic friction angle	ϕ^*_{ini}	[º]	25
Peak asymptotic friction angle	ϕ^*_{peak}	[º]	29.4
Residual friction angle	ϕ^*_{res}	[º]	15
Asymptotic cohesion (mean value)	c^*_{ini}	[kPa]	35
Tensile strength	$p_{\text{t ini}}$	[kPa]	0
Equivalent strain at peak strength	χ	[-]	0.009
Constant in hardening law	a_ϕ	[-]	0.005
Rate of reduction of friction angle	b_ϕ	[-]	0.05
Rate of reduction of cohesion	b_c	[-]	15
Non-associative constant	ω	[-]	0.8
Length scale parameter	l_s	[cm]	1.0

Figure 1

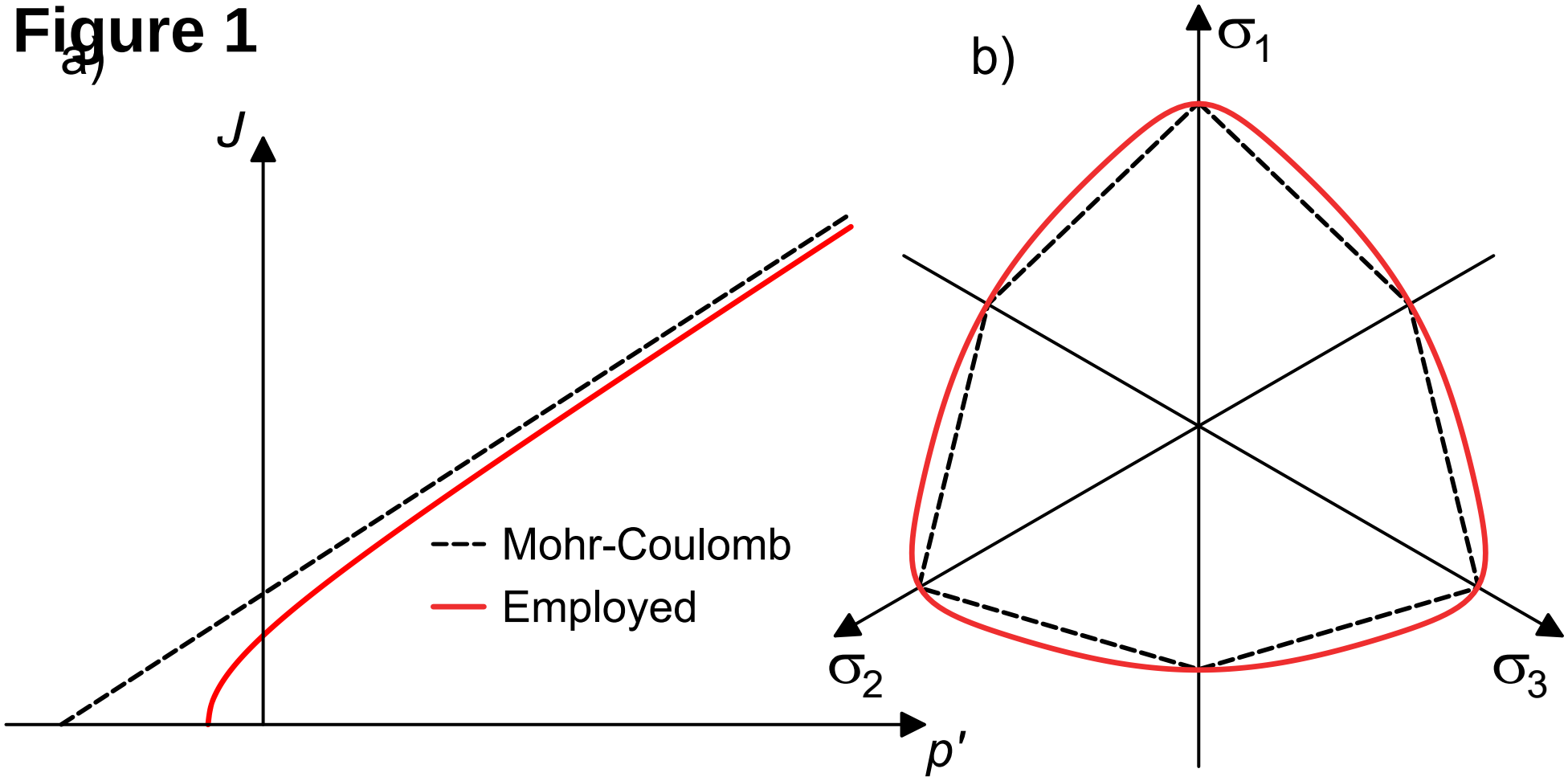

Figure 2

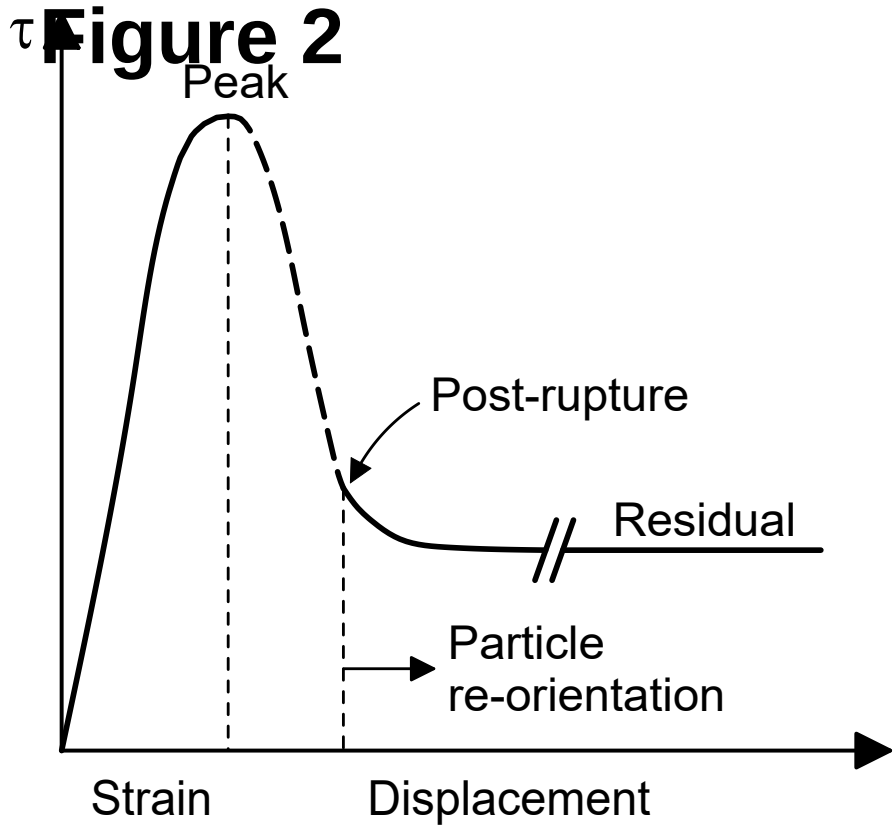
τ
Peak
Post-rupture
Residual
Particle
re-orientation
Strain
Displacement

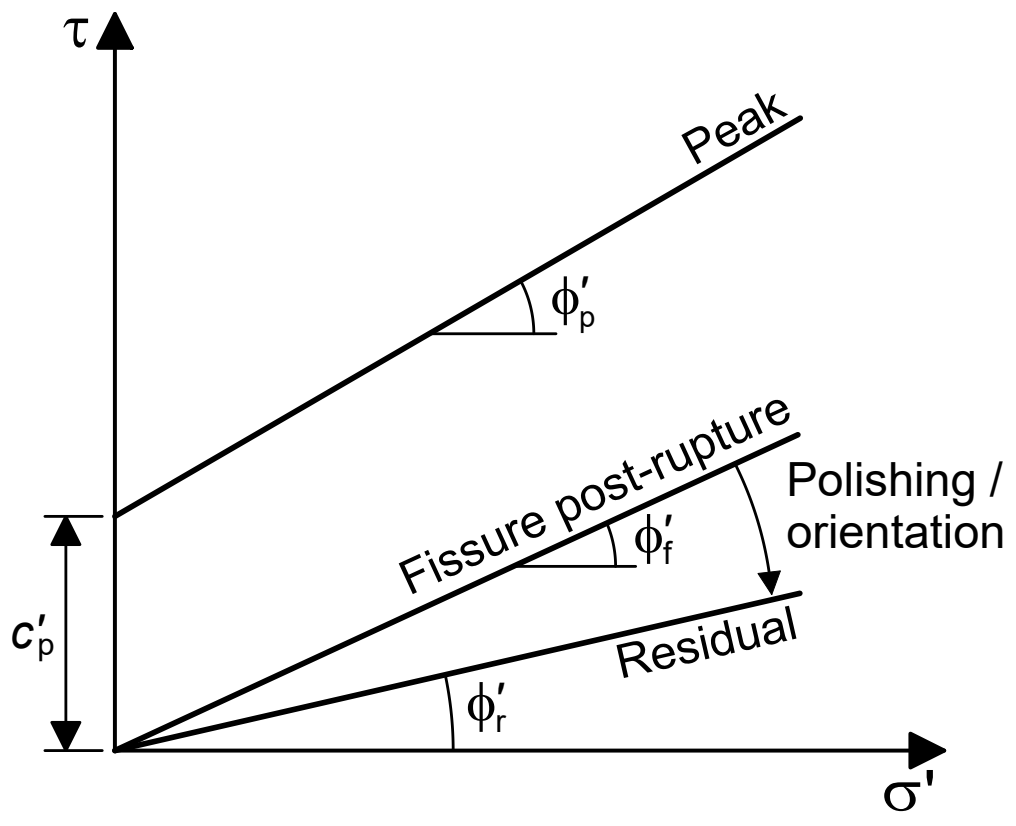
τ
Peak
ϕ'_p
Fissure post-rupture
ϕ'_f
Polishing /
orientation
c'_p
Residual
ϕ'_r
σ'

Figure 3

$$\tan\phi^* = \tan\phi^*_{\text{ini}} + \frac{\varepsilon^{\text{p}}_{\text{eq}}}{a_\phi + \frac{\varepsilon^{\text{p}}_{\text{eq}}}{\Delta}} \qquad \Delta = \frac{\chi}{\frac{\chi}{\tan\phi^*_{\text{peak}} - \tan\phi^*_{\text{ini}}} - a_\phi}$$

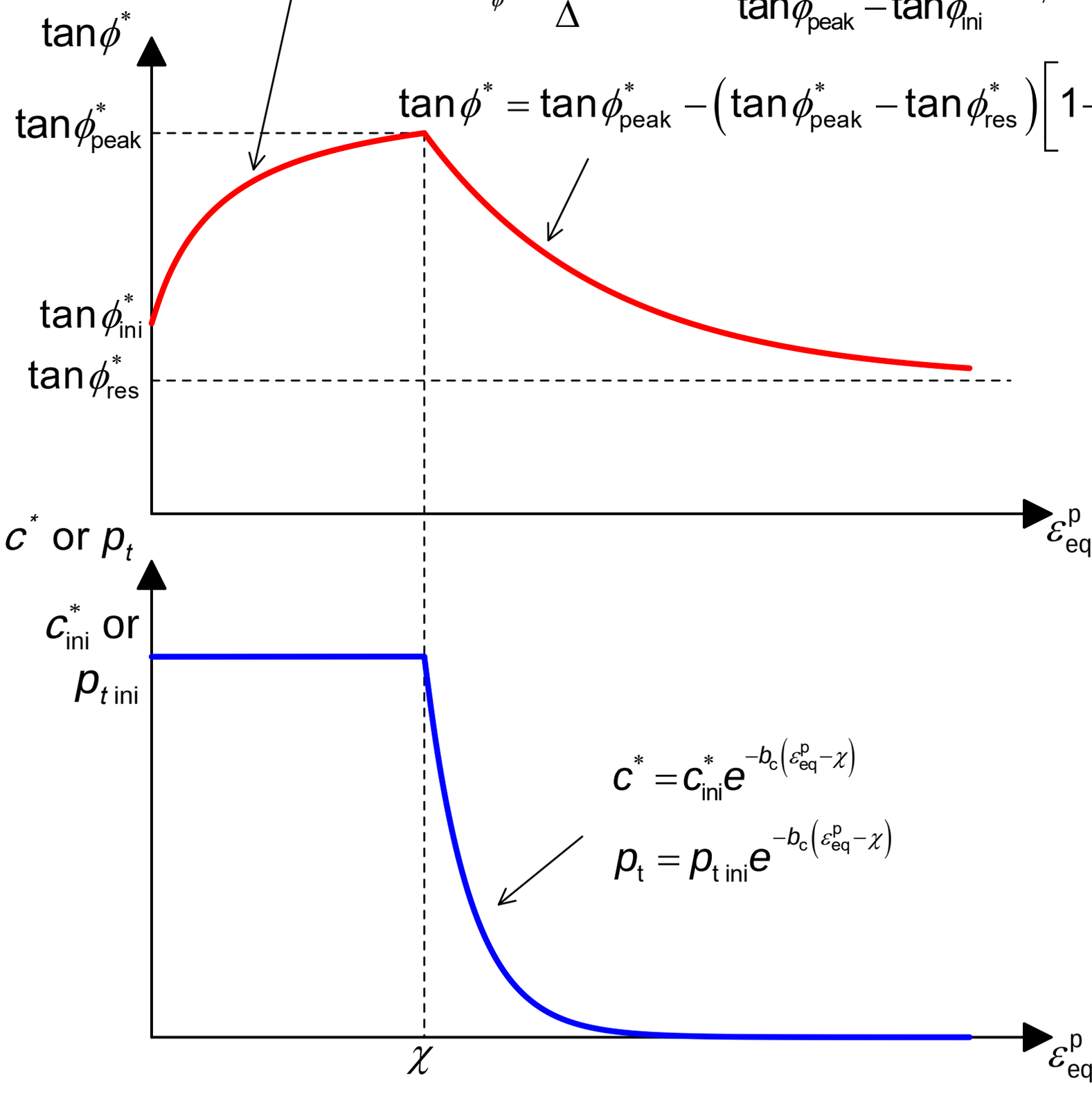

$$\tan\phi^* = \tan\phi^*_{\text{peak}} - \left(\tan\phi^*_{\text{peak}} - \tan\phi^*_{\text{res}}\right)\left[1 - e^{-b_\phi\left(\varepsilon^{\text{p}}_{\text{eq}} - \chi\right)}\right]$$

$$c^* = c^*_{\text{ini}} e^{-b_{\text{c}}\left(\varepsilon^{\text{p}}_{\text{eq}} - \chi\right)}$$

$$p_{\text{t}} = p_{\text{t ini}} e^{-b_{\text{c}}\left(\varepsilon^{\text{p}}_{\text{eq}} - \chi\right)}$$

Figure 4

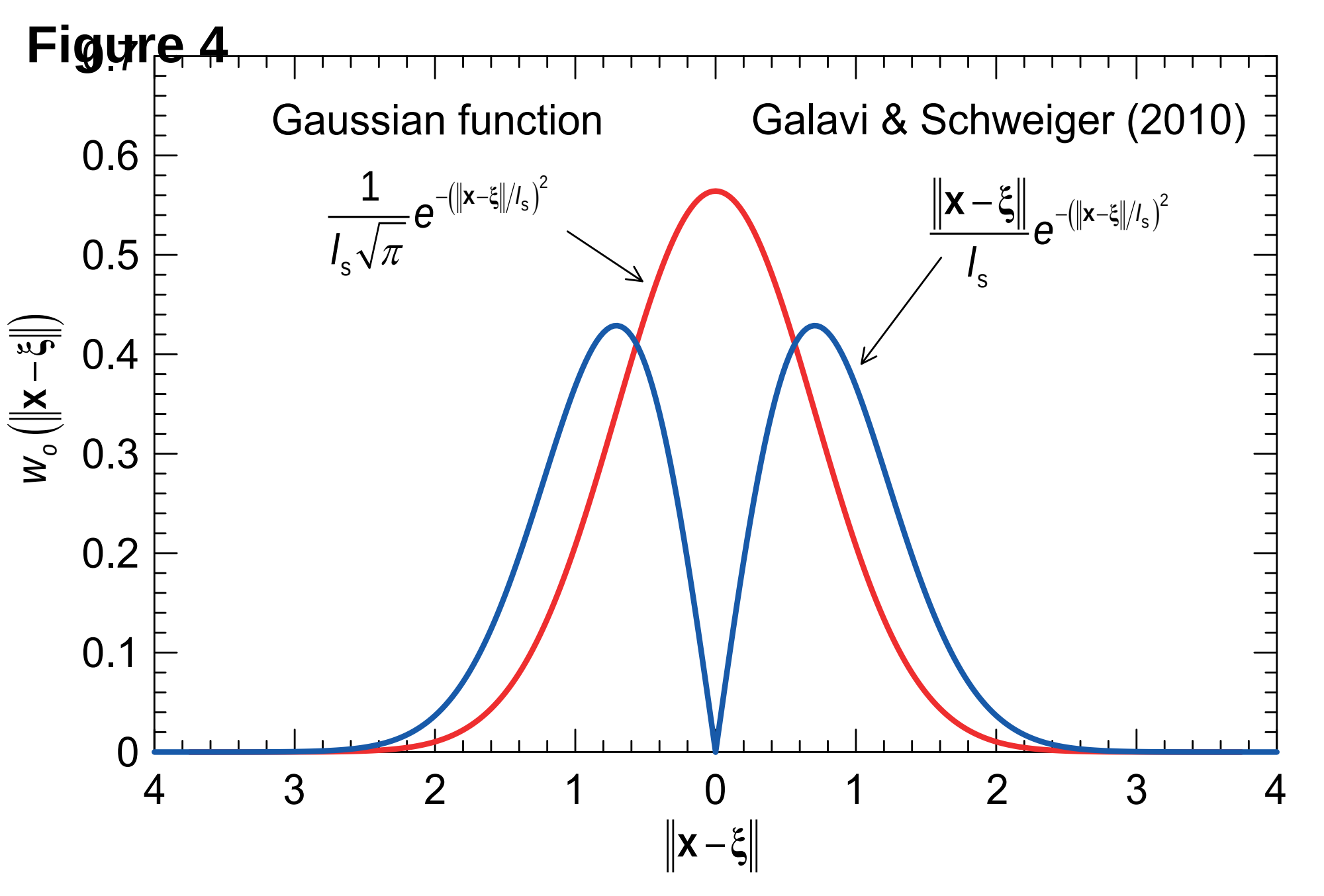
Gaussian function
Galavi & Schweiger (2010)
$\frac{1}{l_s\sqrt{\pi}} e^{-(\|\mathbf{x}-\boldsymbol{\xi}\|/l_s)^2}$
$\frac{\|\mathbf{x}-\boldsymbol{\xi}\|}{l_s} e^{-(\|\mathbf{x}-\boldsymbol{\xi}\|/l_s)^2}$
$w_o(\|\mathbf{x}-\boldsymbol{\xi}\|)$
$\|\mathbf{x}-\boldsymbol{\xi}\|$
0.7
0.6
0.5
0.4
0.3
0.2
0.1
0
4
3
2
1
0
1
2
3
4

Figure 5

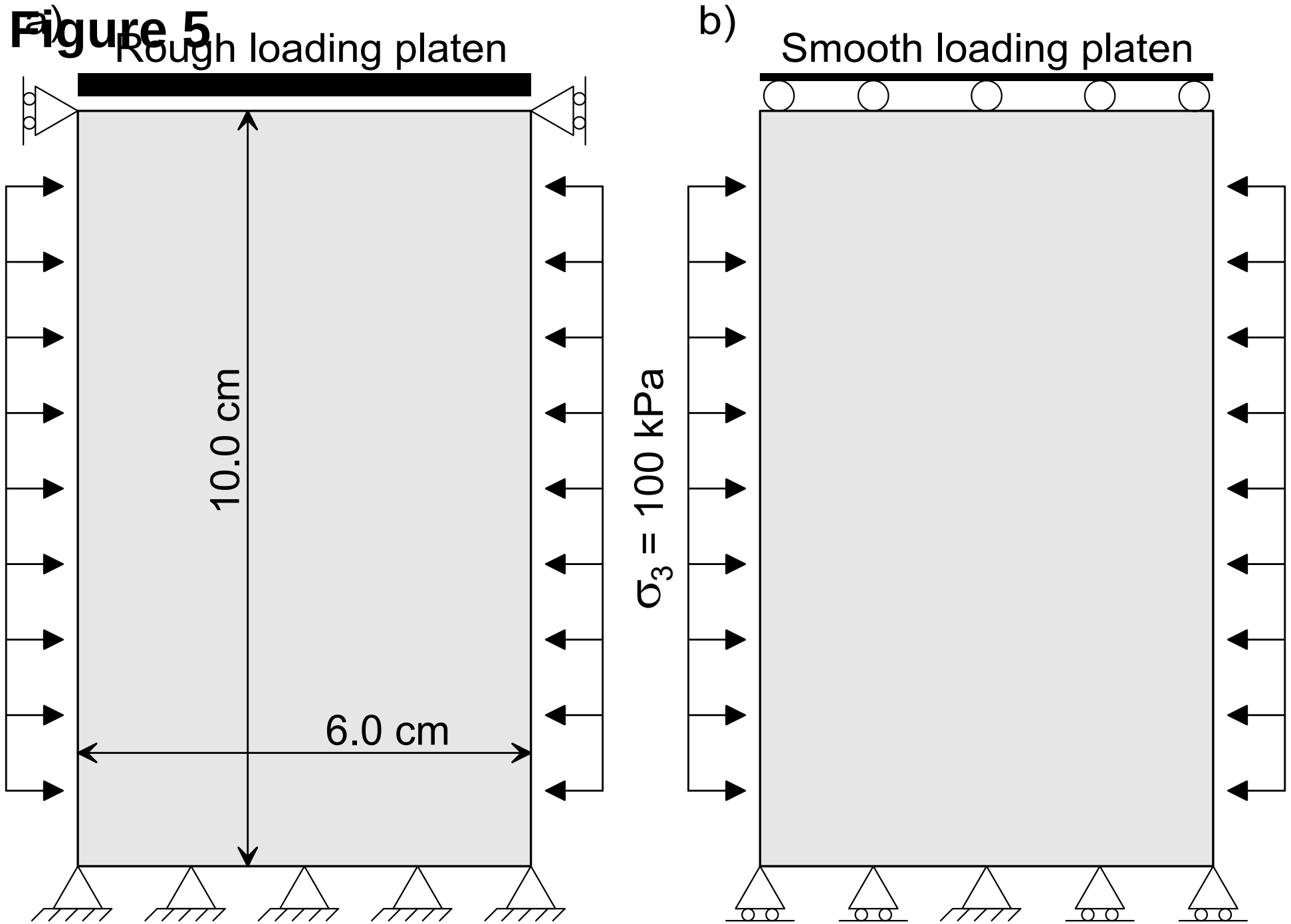
a)
Rough loading platen
10.0 cm
6.0 cm
b)
Smooth loading platen
σ_3 = 100 kPa

Figure 6

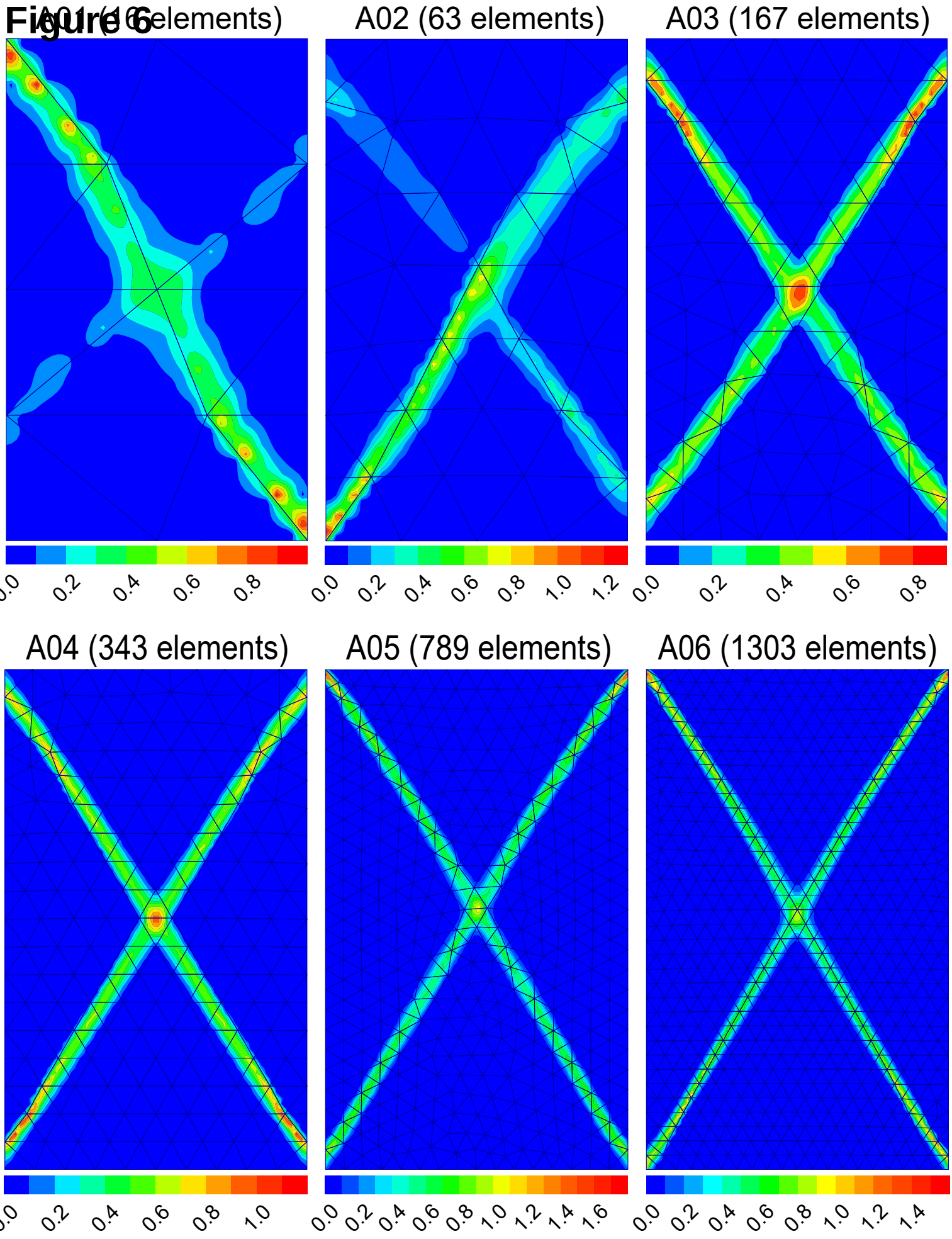
A01 (116 elements)
A02 (63 elements)
A03 (167 elements)
0.0 0.2 0.4 0.6 0.8
0.0 0.2 0.4 0.6 0.8 1.0 1.2
0.0 0.2 0.4 0.6 0.8
A04 (343 elements)
A05 (789 elements)
A06 (1303 elements)
0.0 0.2 0.4 0.6 0.8 1.0
0.0 0.2 0.4 0.6 0.8 1.0 1.2 1.4 1.6
0.0 0.2 0.4 0.6 0.8 1.0 1.2 1.4

Figure 7

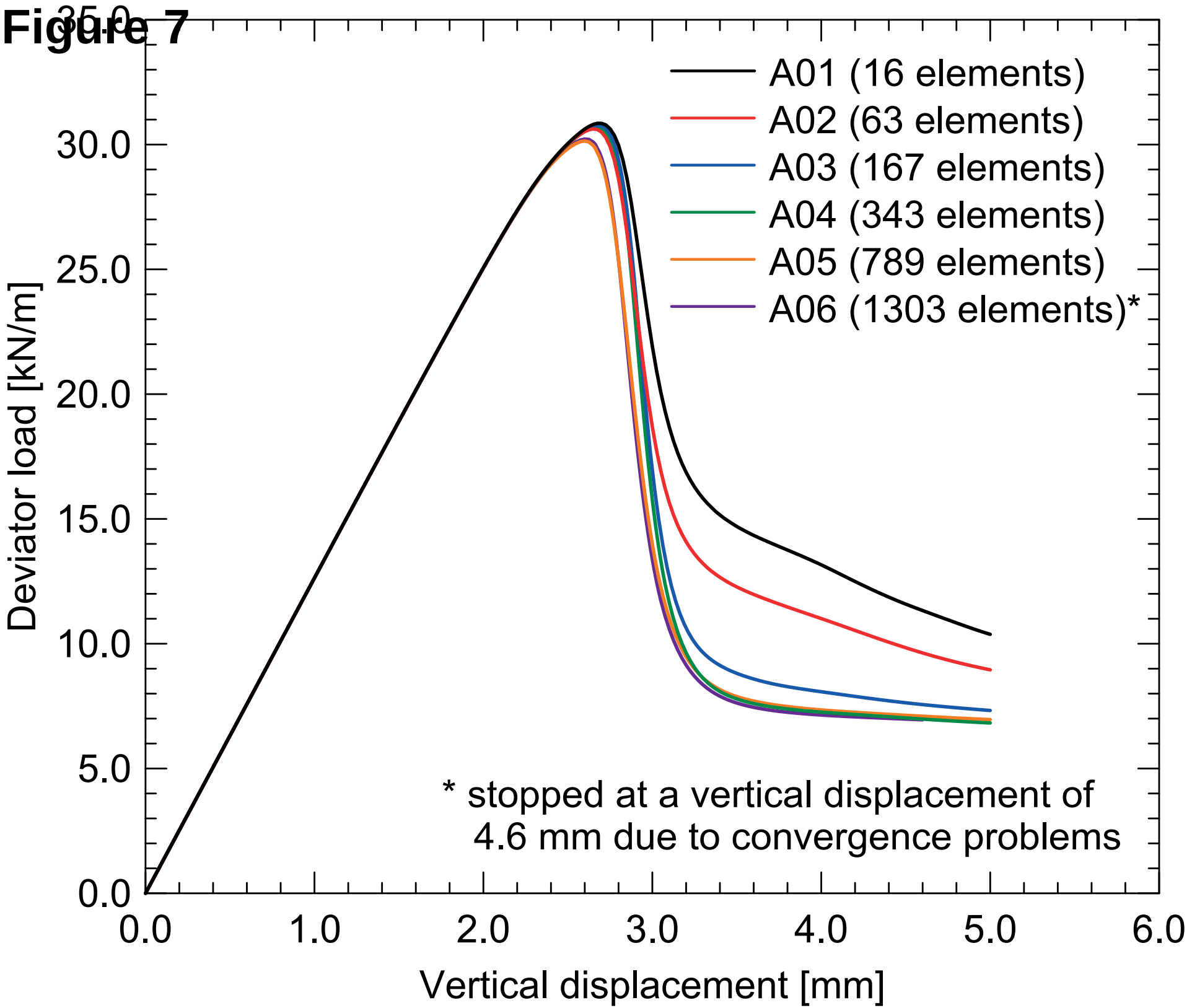
A01 (16 elements)
A02 (63 elements)
A03 (167 elements)
A04 (343 elements)
A05 (789 elements)
A06 (1303 elements)*
* stopped at a vertical displacement of
4.6 mm due to convergence problems
Deviator load [kN/m]
Vertical displacement [mm]
0.0
5.0
10.0
15.0
20.0
25.0
30.0
35.0
0.0
1.0
2.0
3.0
4.0
5.0
6.0

Figure 8

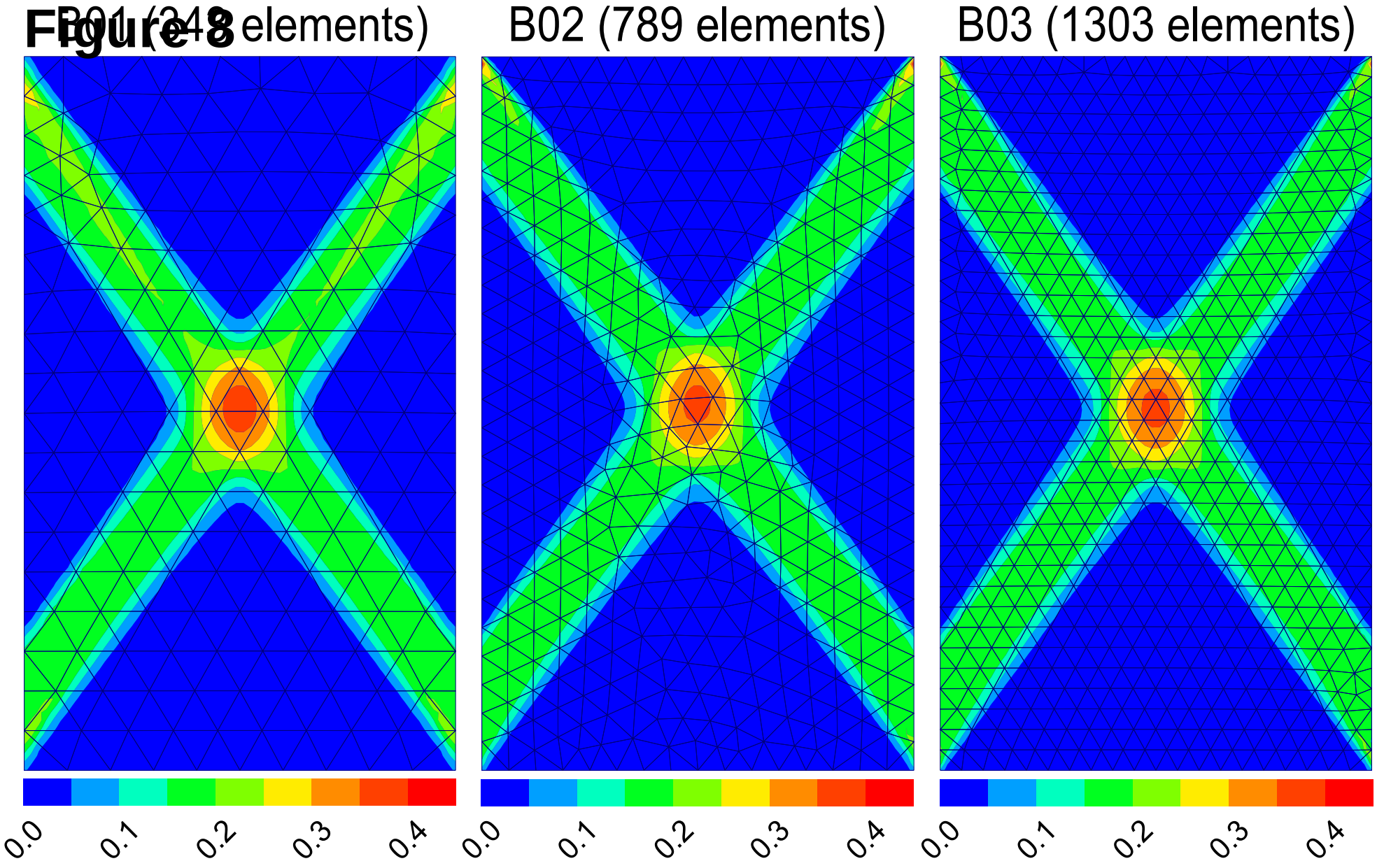
B01 (348 elements)
B02 (789 elements)
B03 (1303 elements)
0.0
0.1
0.2
0.3
0.4
0.0
0.1
0.2
0.3
0.4
0.0
0.1
0.2
0.3
0.4

Figure 9

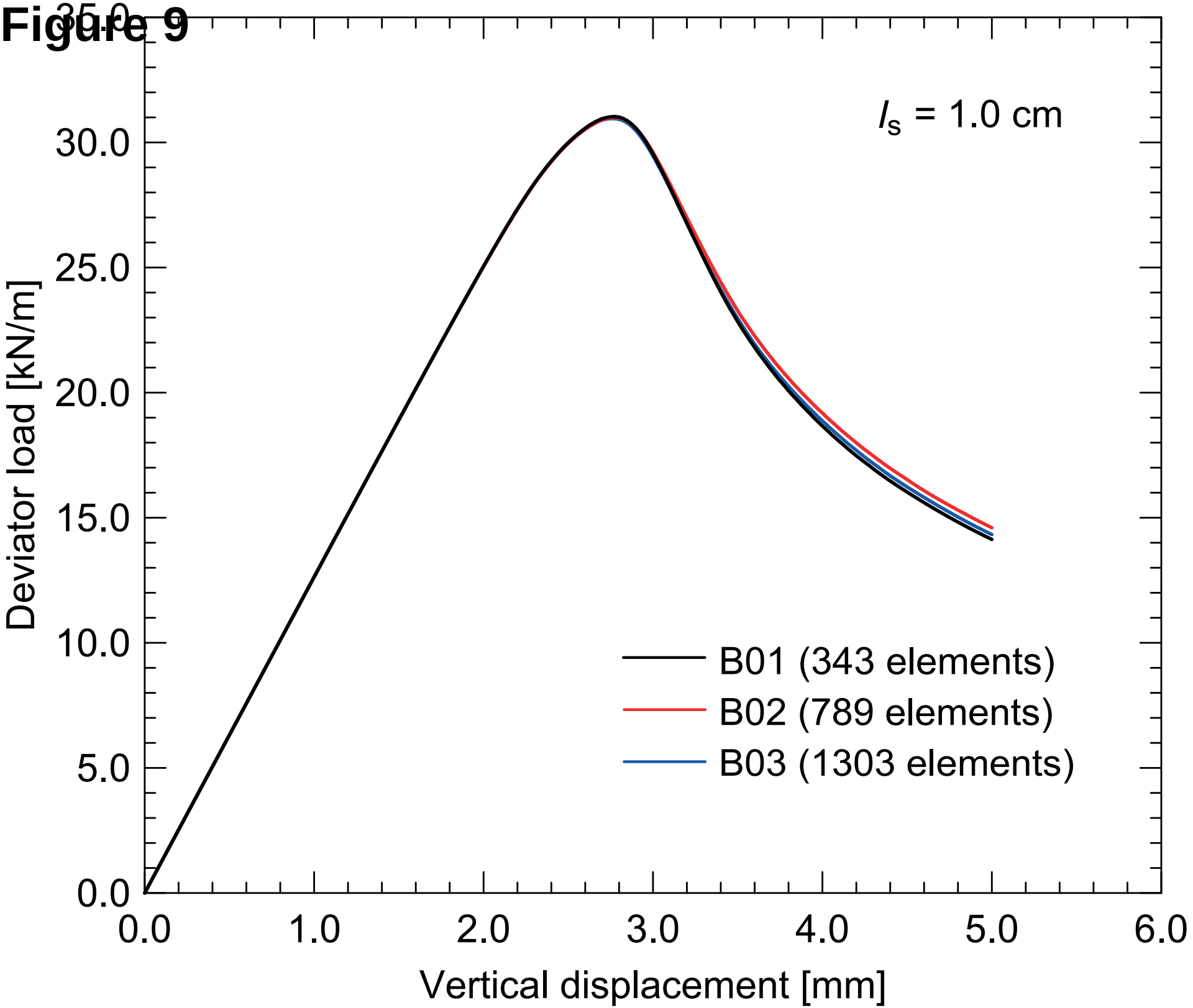
l_s = 1.0 cm
B01 (343 elements)
B02 (789 elements)
B03 (1303 elements)
Deviator load [kN/m]
Vertical displacement [mm]
0.0
5.0
10.0
15.0
20.0
25.0
30.0
35.0
0.0
1.0
2.0
3.0
4.0
5.0
6.0

Figure 10

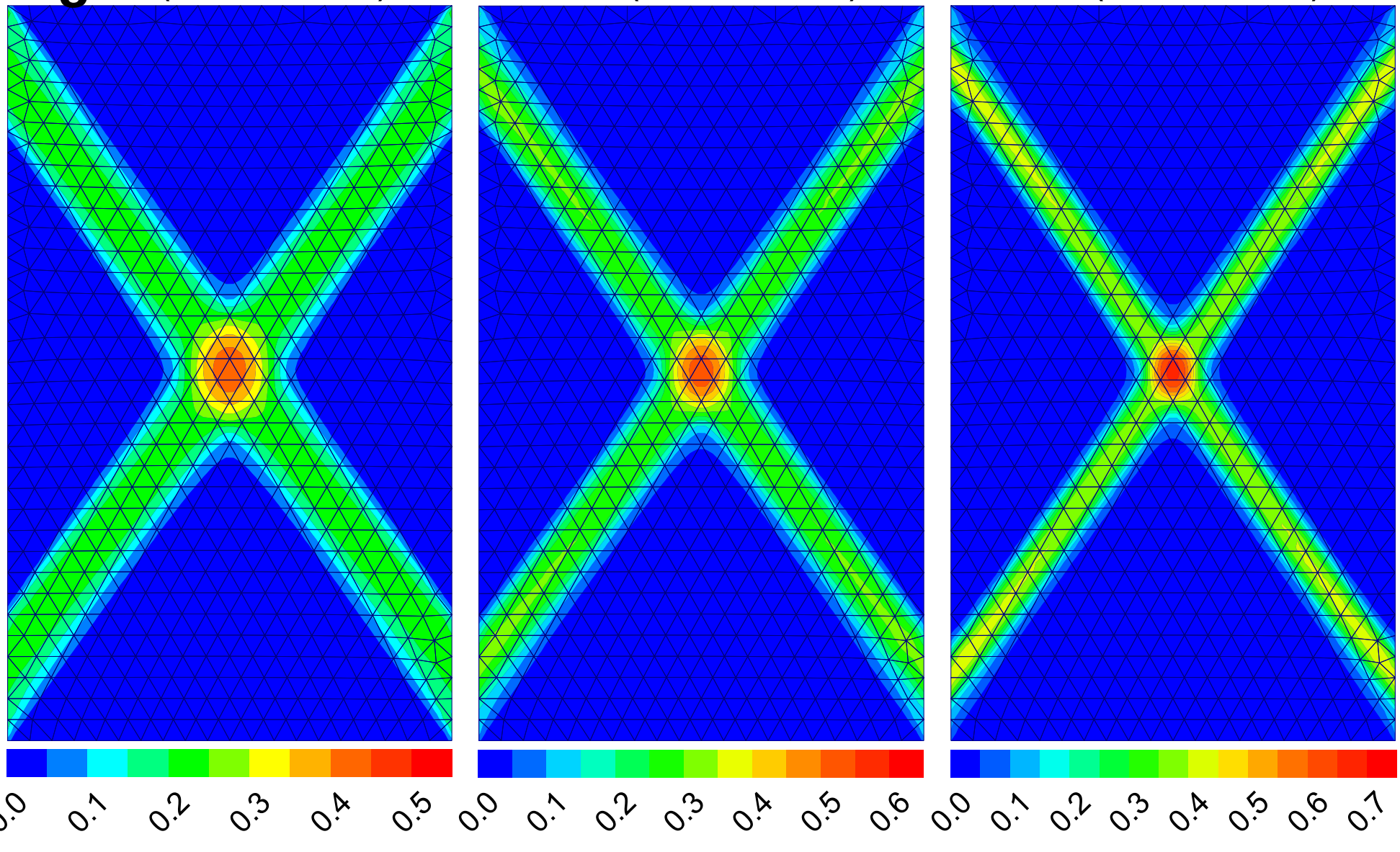
C01 (l_s = 0.8 cm)
C02 (l_s = 0.6 cm)
C03 (l_s = 0.4 cm)
0.0 0.1 0.2 0.3 0.4 0.5
0.0 0.1 0.2 0.3 0.4 0.5 0.6
0.0 0.1 0.2 0.3 0.4 0.5 0.6 0.7

Figure 11

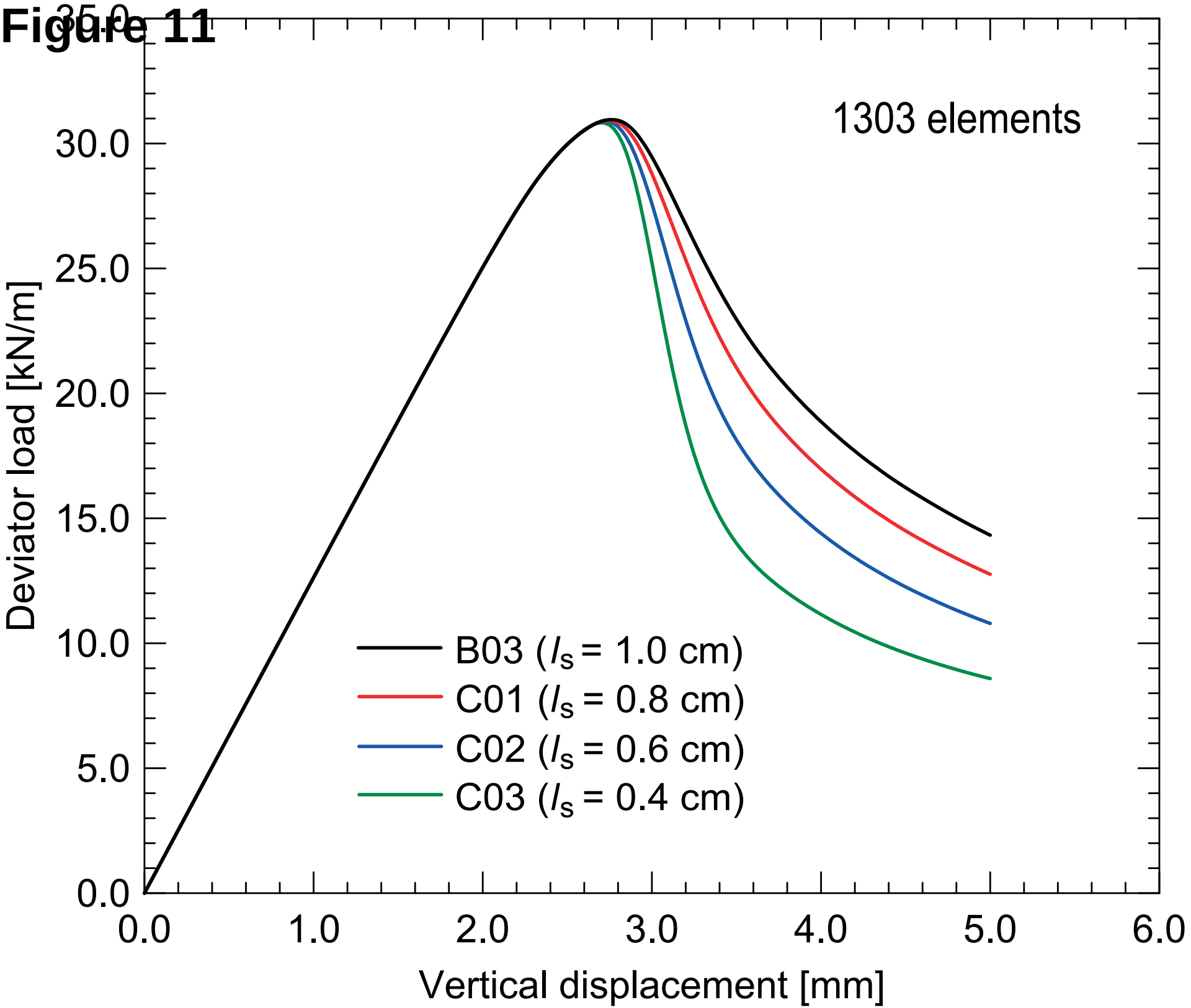
1303 elements
Deviator load [kN/m]
Vertical displacement [mm]
0.0
5.0
10.0
15.0
20.0
25.0
30.0
35.0
0.0
1.0
2.0
3.0
4.0
5.0
6.0
B03 (l_s = 1.0 cm)
C01 (l_s = 0.8 cm)
C02 (l_s = 0.6 cm)
C03 (l_s = 0.4 cm)

Figure 12

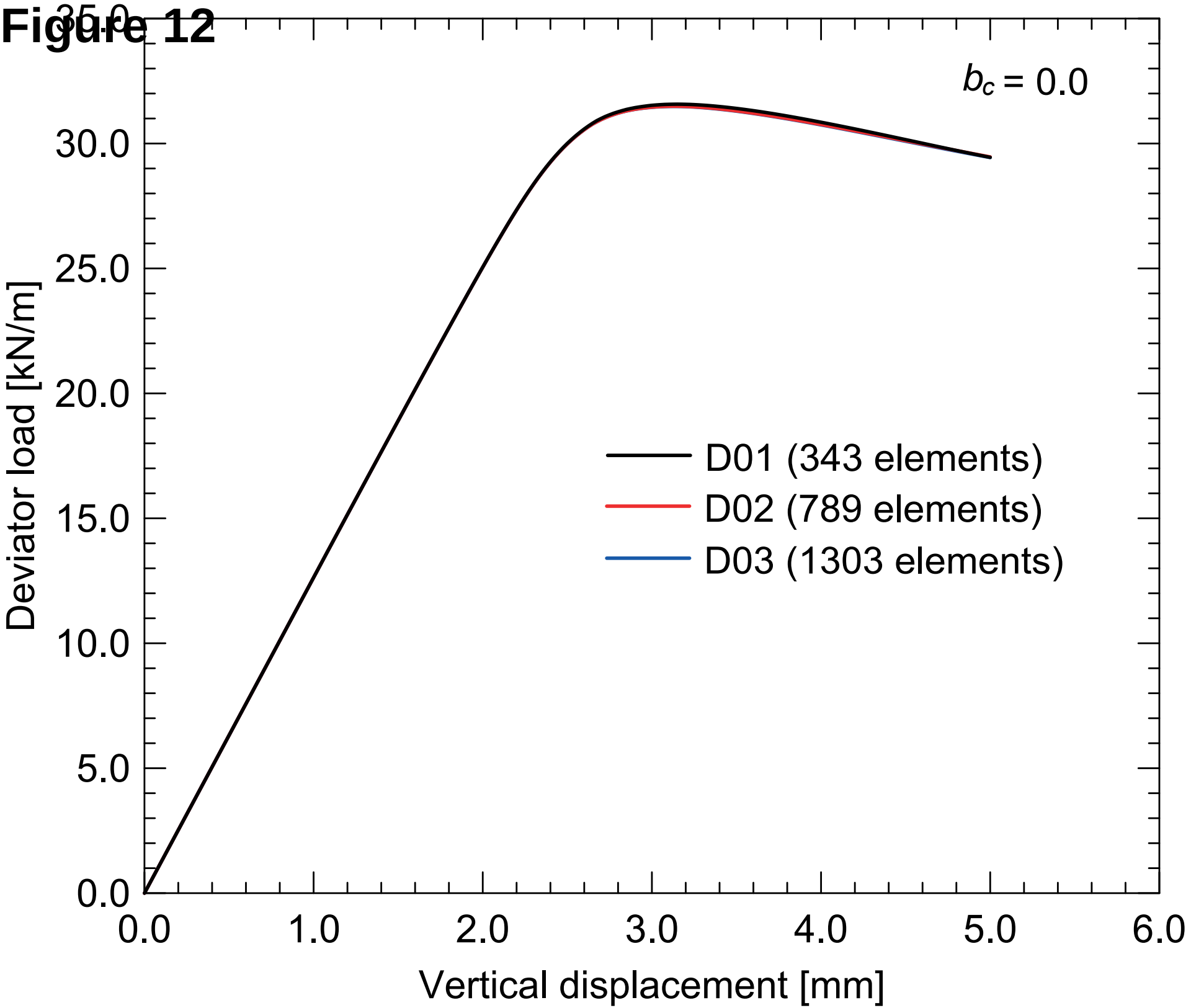
b_c = 0.0
D01 (343 elements)
D02 (789 elements)
D03 (1303 elements)
Deviator load [kN/m]
Vertical displacement [mm]
0.0
5.0
10.0
15.0
20.0
25.0
30.0
35.0
0.0
1.0
2.0
3.0
4.0
5.0
6.0

Figure 13

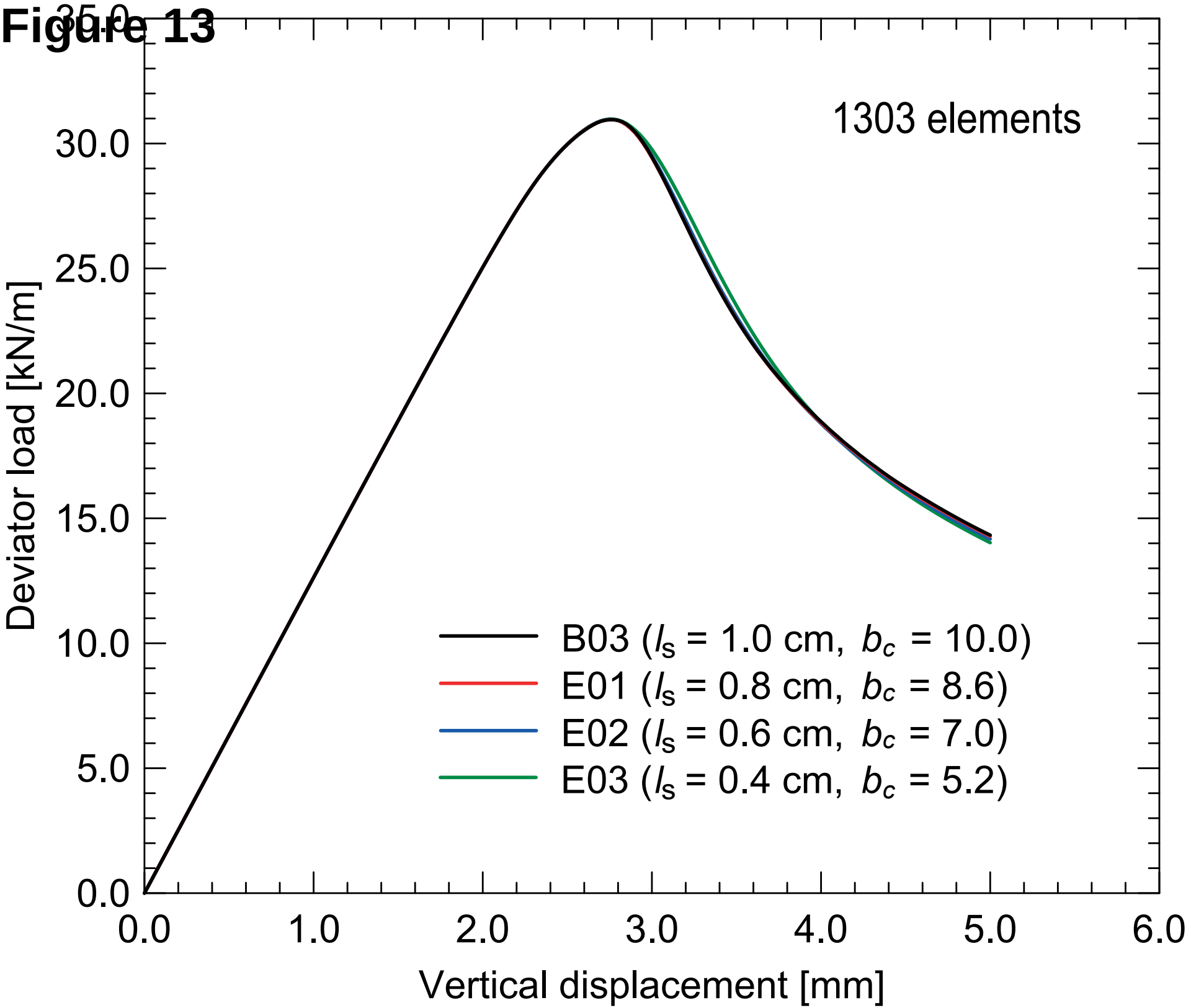
1303 elements
Deviator load [kN/m]
Vertical displacement [mm]
0.0
5.0
10.0
15.0
20.0
25.0
30.0
35.0
0.0
1.0
2.0
3.0
4.0
5.0
6.0
B03 (l_s = 1.0 cm, b_c = 10.0)
E01 (l_s = 0.8 cm, b_c = 8.6)
E02 (l_s = 0.6 cm, b_c = 7.0)
E03 (l_s = 0.4 cm, b_c = 5.2)

Figure 14

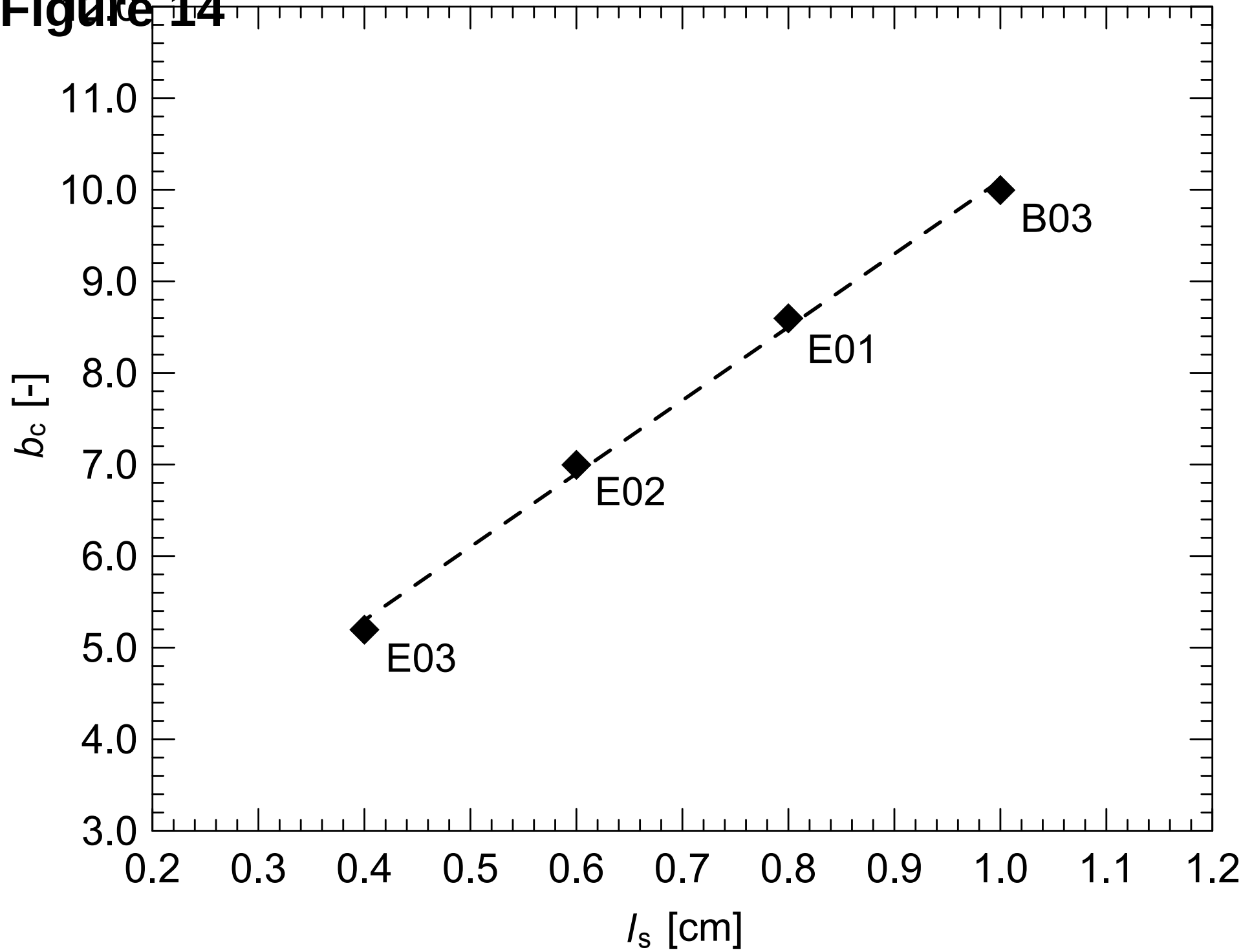
11.0
10.0
9.0
8.0
7.0
6.0
5.0
4.0
3.0
b_c [-]
0.2
0.3
0.4
0.5
0.6
0.7
0.8
0.9
1.0
1.1
1.2
l_s [cm]
B03
E01
E02
E03

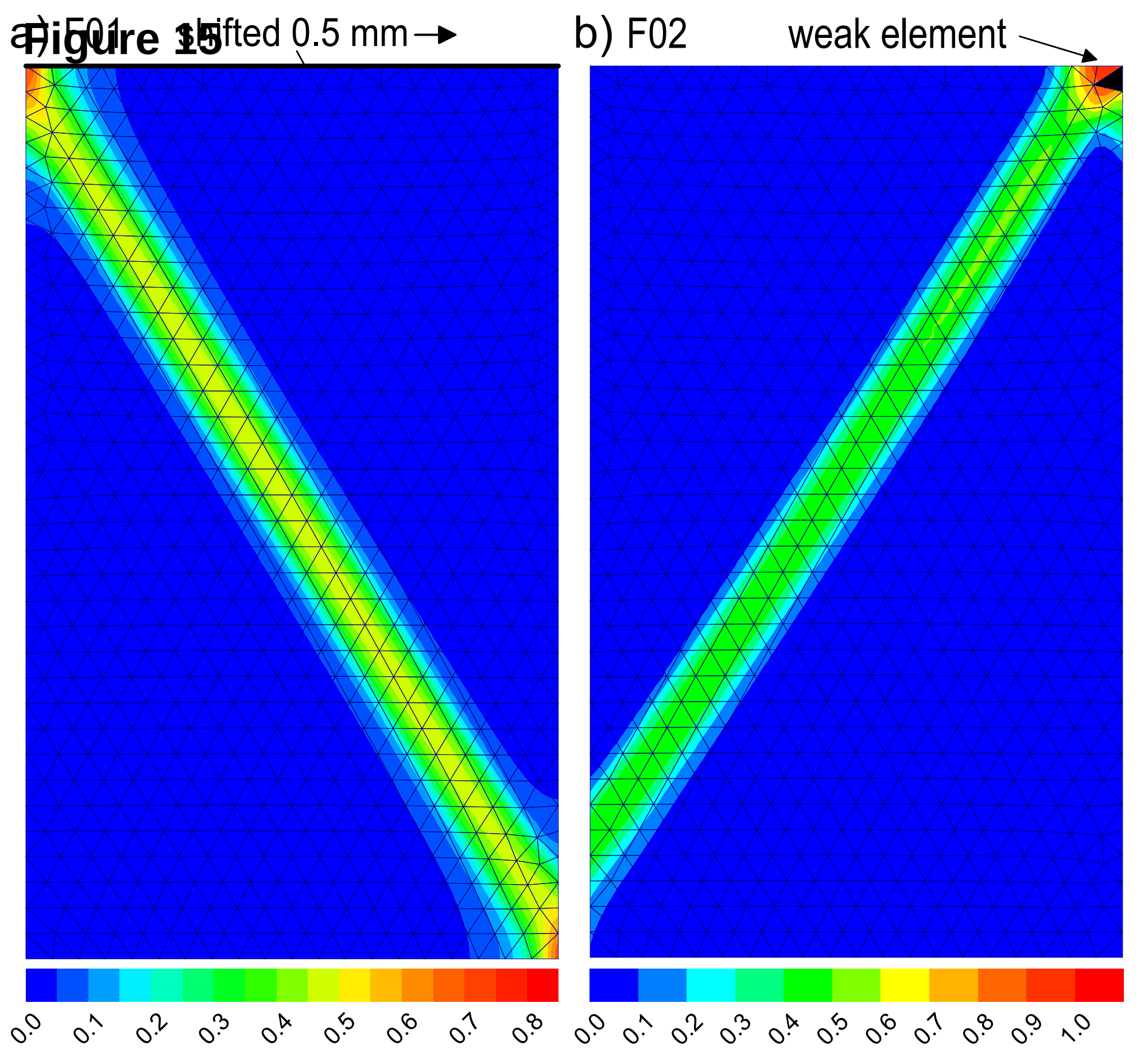
a) F01
shifted 0.5 mm
b) F02
weak element
0.0
0.1
0.2
0.3
0.4
0.5
0.6
0.7
0.8
0.0
0.1
0.2
0.3
0.4
0.5
0.6
0.7
0.8
0.9
1.0

Figure 15

Figure 16

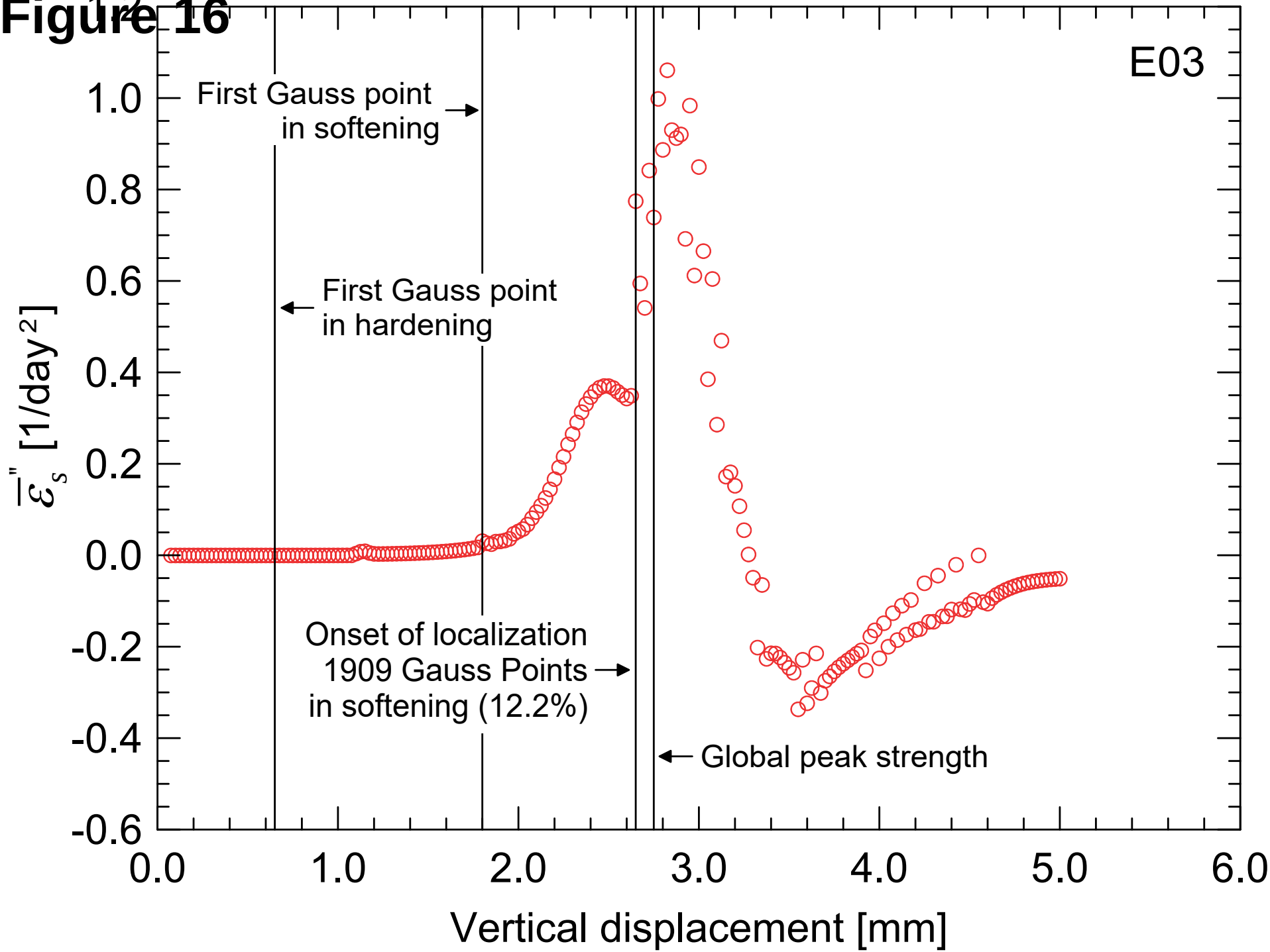
E03
First Gauss point
in softening
First Gauss point
in hardening
Onset of localization
1909 Gauss Points
in softening (12.2%)
Global peak strength
$\overline{\varepsilon}_s''$ [1/day^2]
Vertical displacement [mm]
1.2
1.0
0.8
0.6
0.4
0.2
0.0
-0.2
-0.4
-0.6
0.0
1.0
2.0
3.0
4.0
5.0
6.0

Figure 17

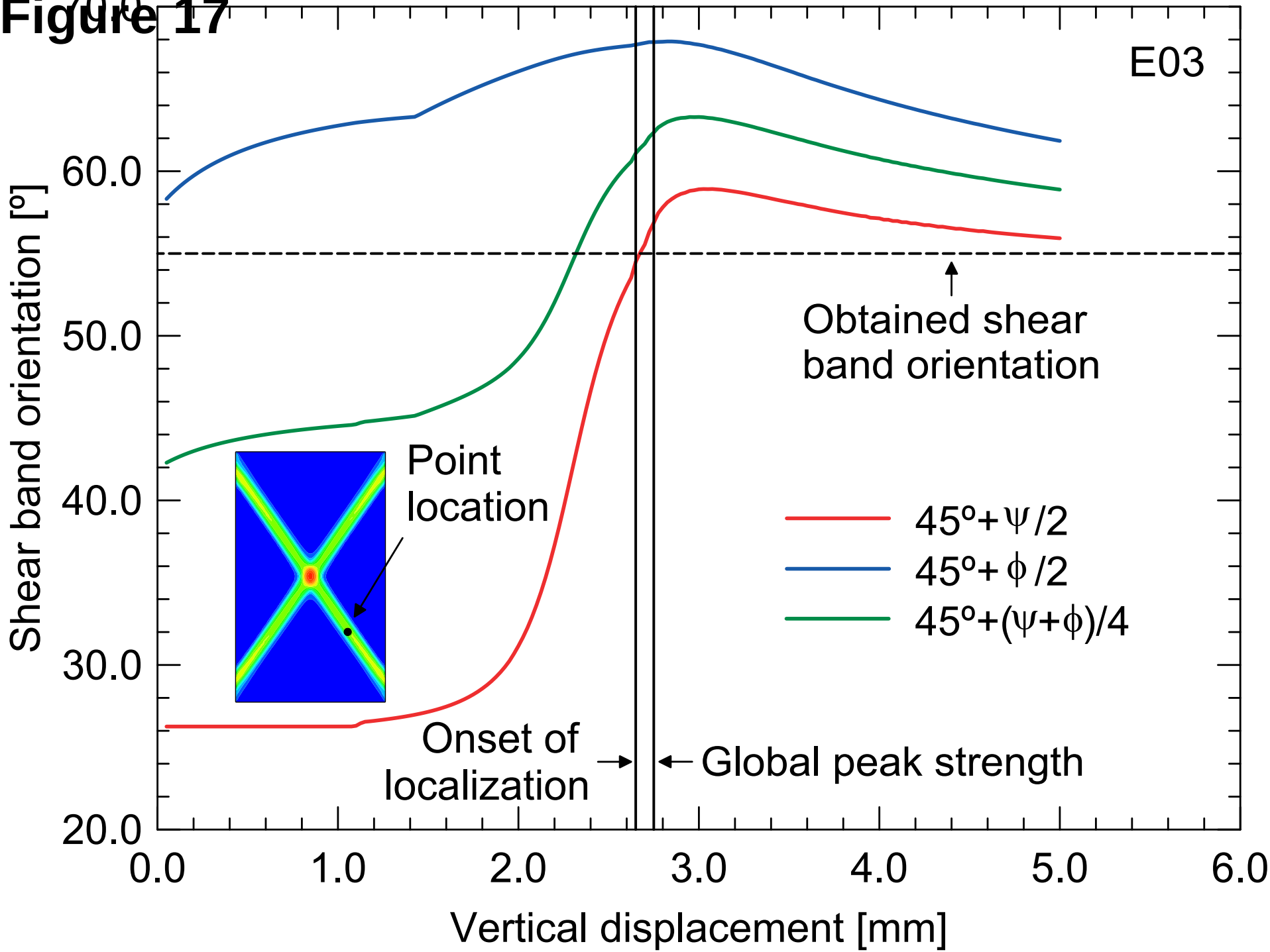
E03
Shear band orientation [º]
70.0
60.0
50.0
40.0
30.0
20.0
0.0
1.0
2.0
3.0
4.0
5.0
6.0
Vertical displacement [mm]
Obtained shear band orientation
Point location
Onset of localization
Global peak strength
45º+ψ/2
45º+ϕ/2
45º+(ψ+ϕ)/4

Figure 18

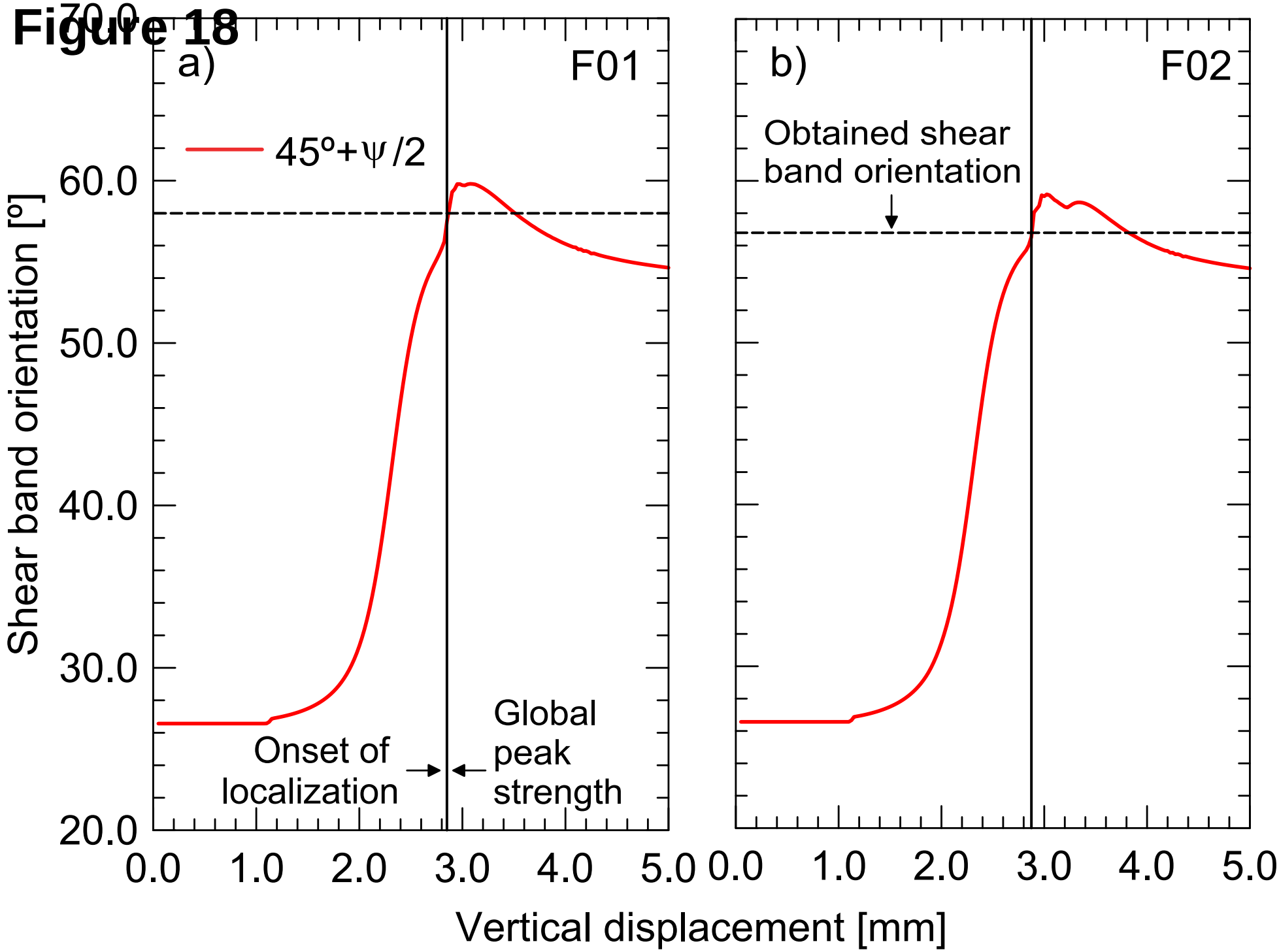
a)
F01
b)
F02
45°+ψ/2
Obtained shear band orientation
Shear band orientation [°]
70.0
60.0
50.0
40.0
30.0
20.0
Onset of localization
Global peak strength
0.0
1.0
2.0
3.0
4.0
5.0
Vertical displacement [mm]

Figure 19

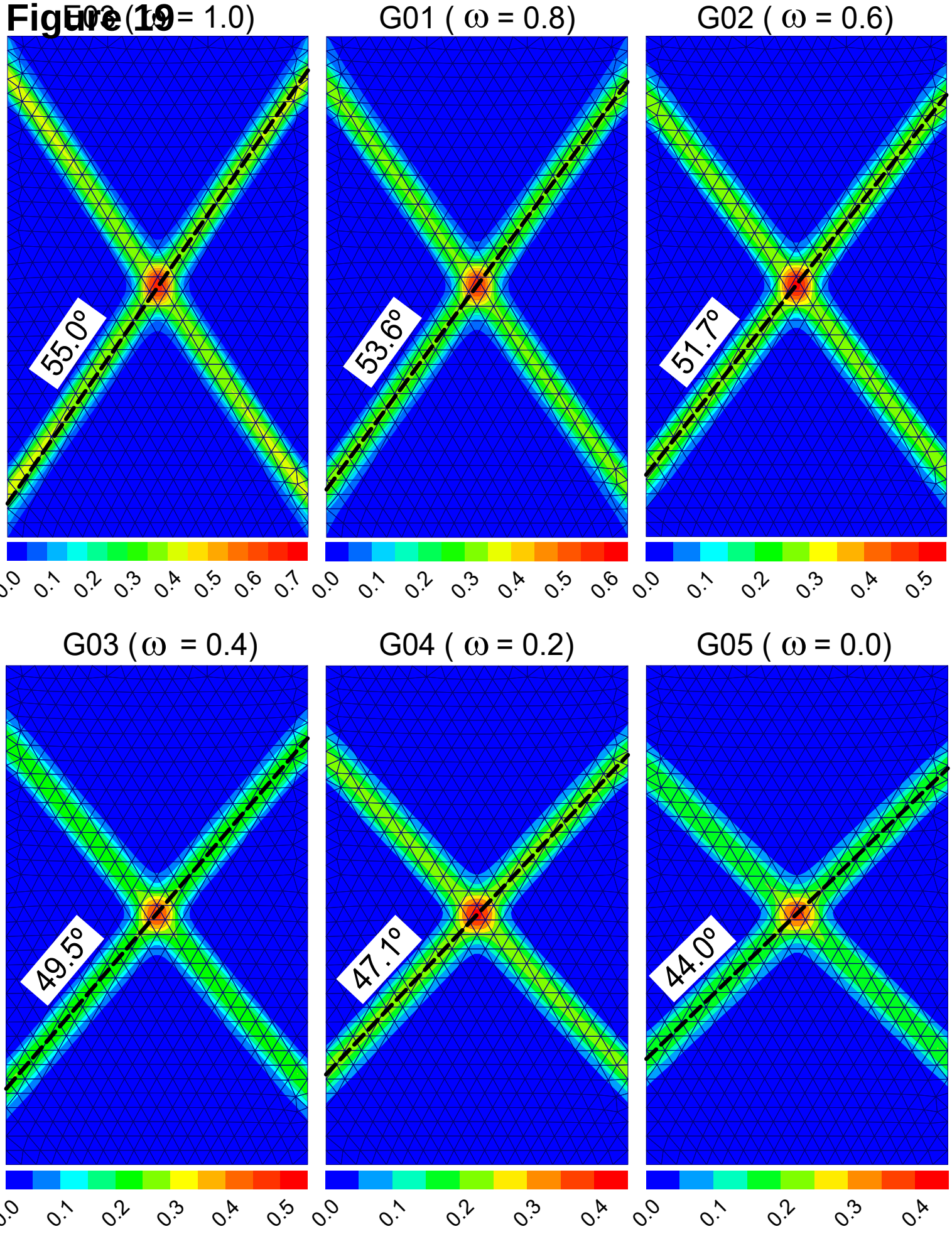
G03 (ω = 1.0)
G01 (ω = 0.8)
G02 (ω = 0.6)
55.0°
53.6°
51.7°
0.0 0.1 0.2 0.3 0.4 0.5 0.6 0.7
0.0 0.1 0.2 0.3 0.4 0.5 0.6
0.0 0.1 0.2 0.3 0.4 0.5
G03 (ω = 0.4)
G04 (ω = 0.2)
G05 (ω = 0.0)
49.5°
47.1°
44.0°
0.0 0.1 0.2 0.3 0.4 0.5
0.0 0.1 0.2 0.3 0.4
0.0 0.1 0.2 0.3 0.4

Figure 20

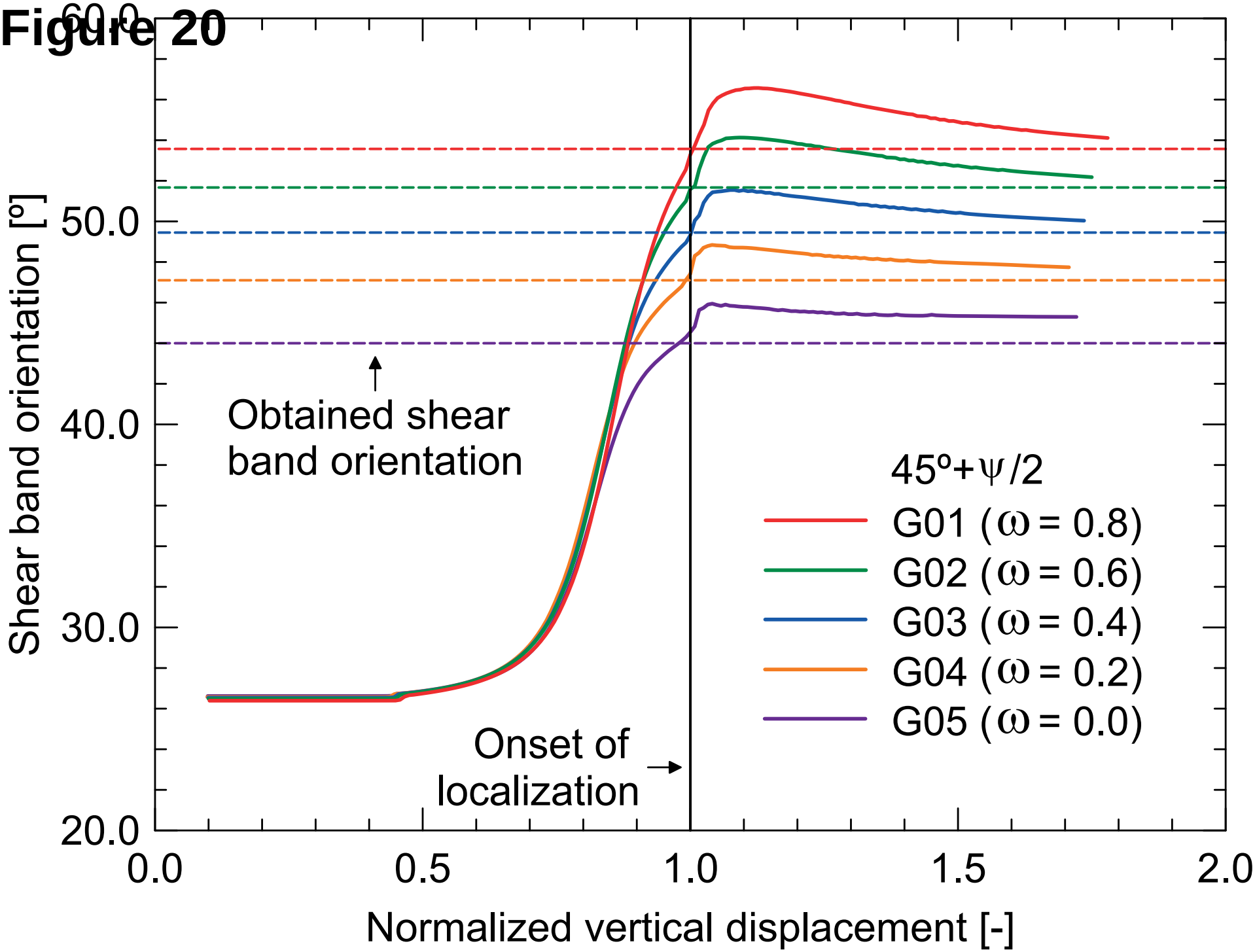
60.0
50.0
40.0
30.0
20.0
Shear band orientation [º]
0.0
0.5
1.0
1.5
2.0
Normalized vertical displacement [-]
Obtained shear band orientation
Onset of localization
45º+ψ/2
G01 (ω = 0.8)
G02 (ω = 0.6)
G03 (ω = 0.4)
G04 (ω = 0.2)
G05 (ω = 0.0)

Figure 21

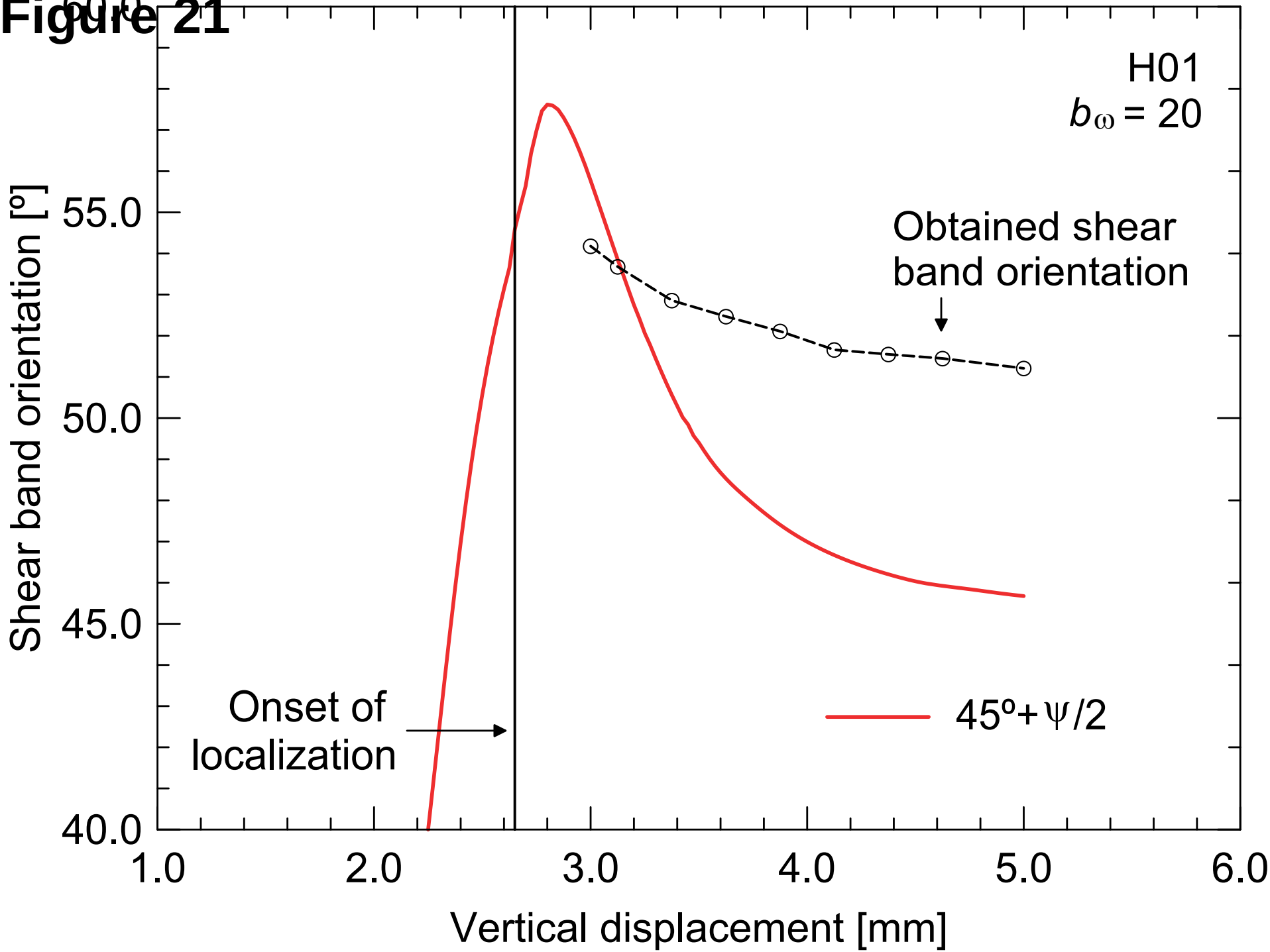
H01
b_ω = 20
Obtained shear band orientation
Onset of localization
45º+ψ/2
Shear band orientation [º]
Vertical displacement [mm]
60.0
55.0
50.0
45.0
40.0
1.0
2.0
3.0
4.0
5.0
6.0

Figure 22

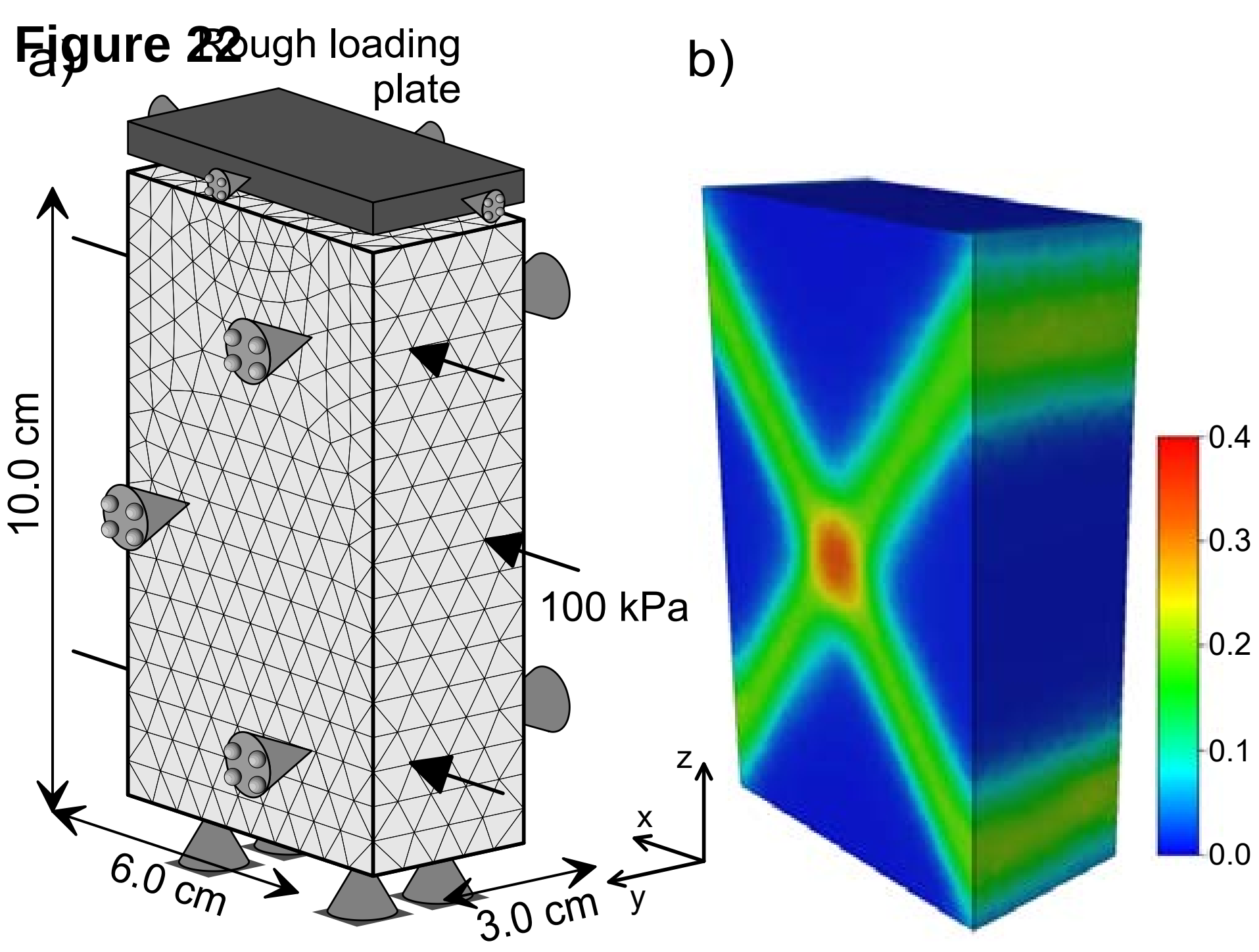
a)
Rough loading plate
10.0 cm
100 kPa
6.0 cm
3.0 cm
z
x
y
b)
0.4
0.3
0.2
0.1
0.0

Figure 23

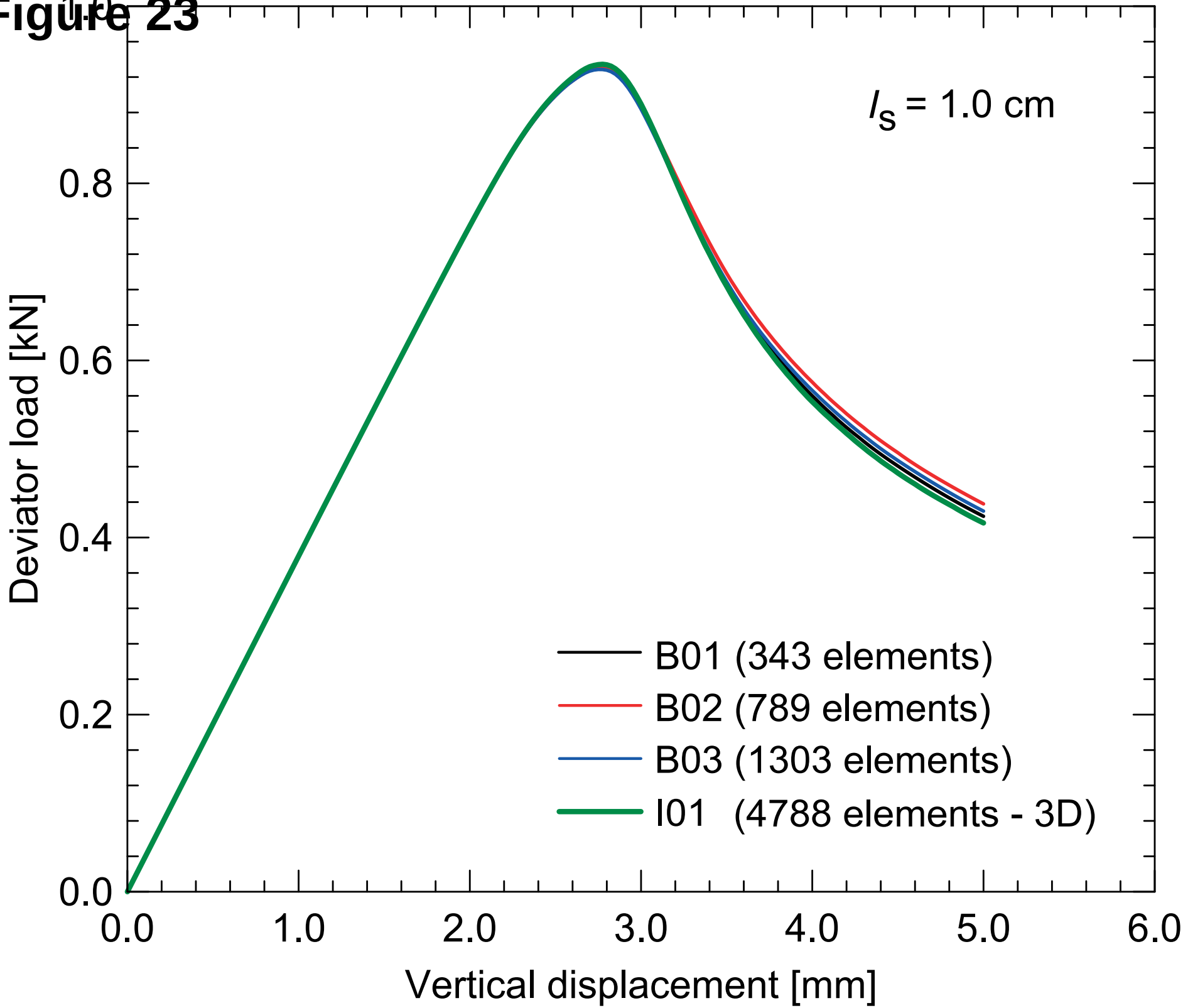
l_s = 1.0 cm
Deviator load [kN]
Vertical displacement [mm]
0.0
0.2
0.4
0.6
0.8
1.0
0.0
1.0
2.0
3.0
4.0
5.0
6.0
B01 (343 elements)
B02 (789 elements)
B03 (1303 elements)
I01 (4788 elements - 3D)

Figure 24

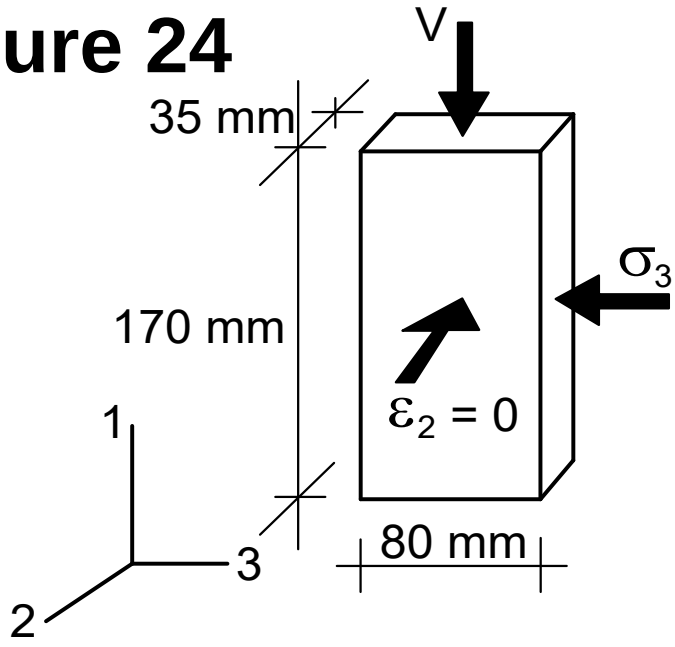

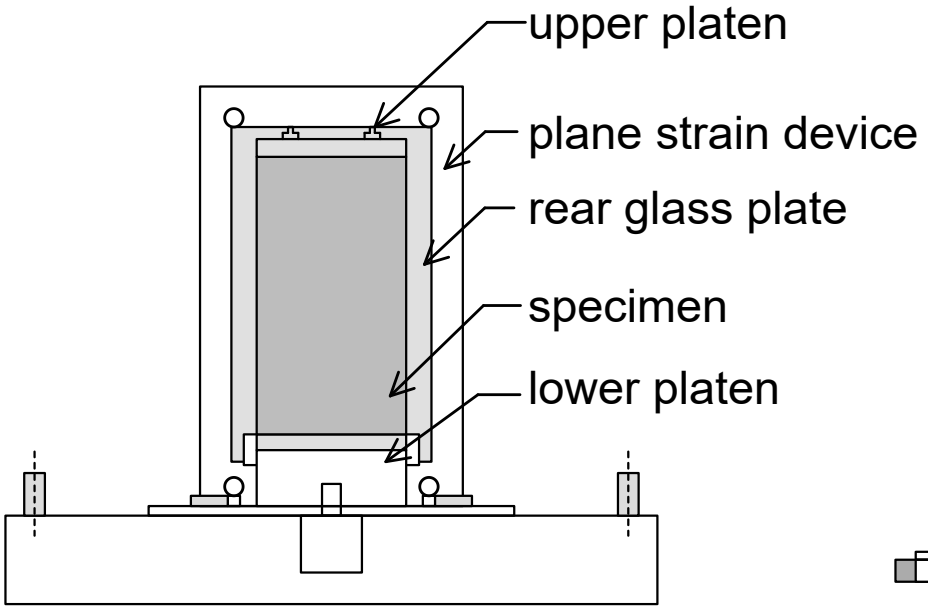

plane strain device and specimen

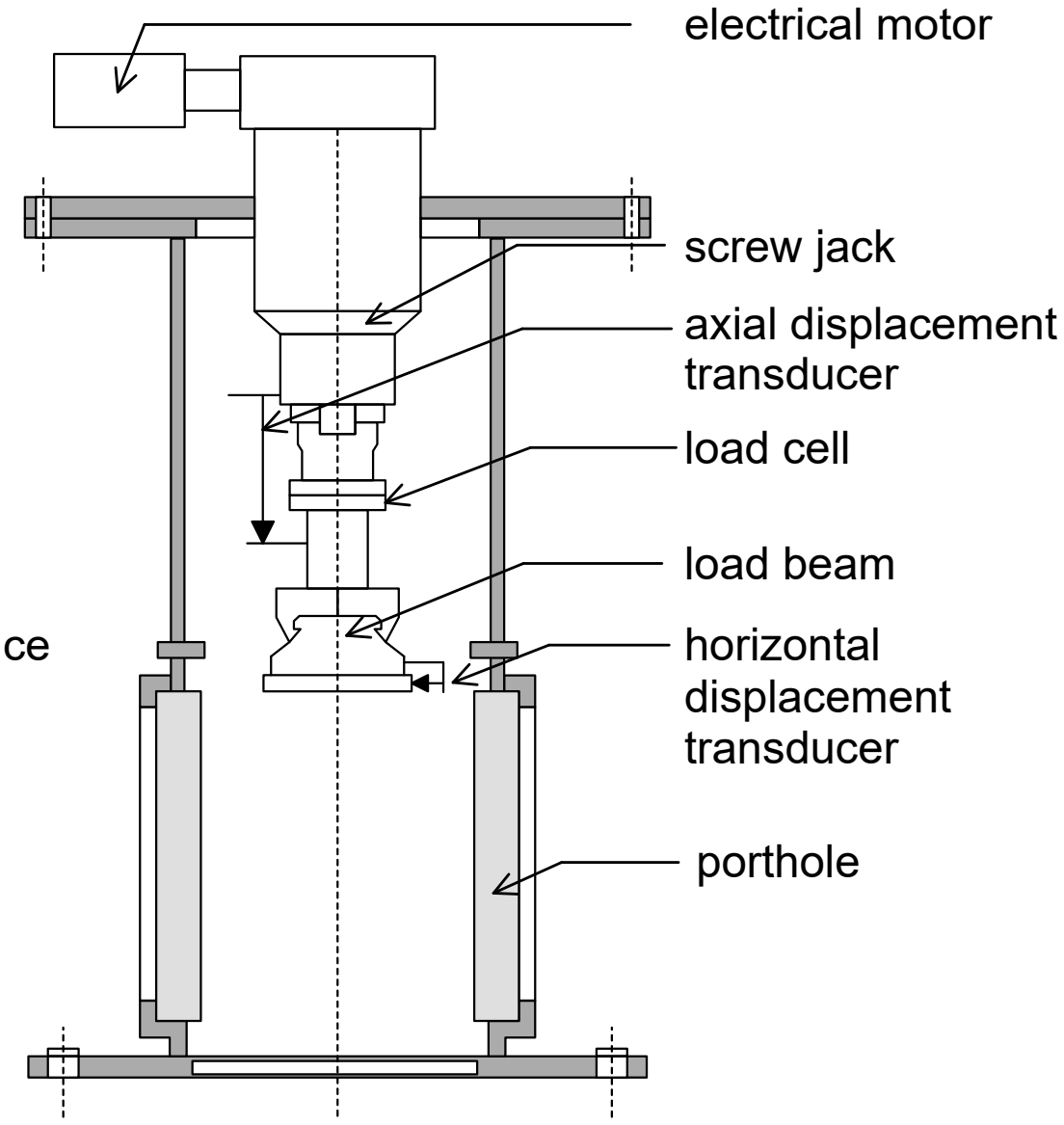

pressure cell and loading device

Figure 25

Click here to download high resolution image

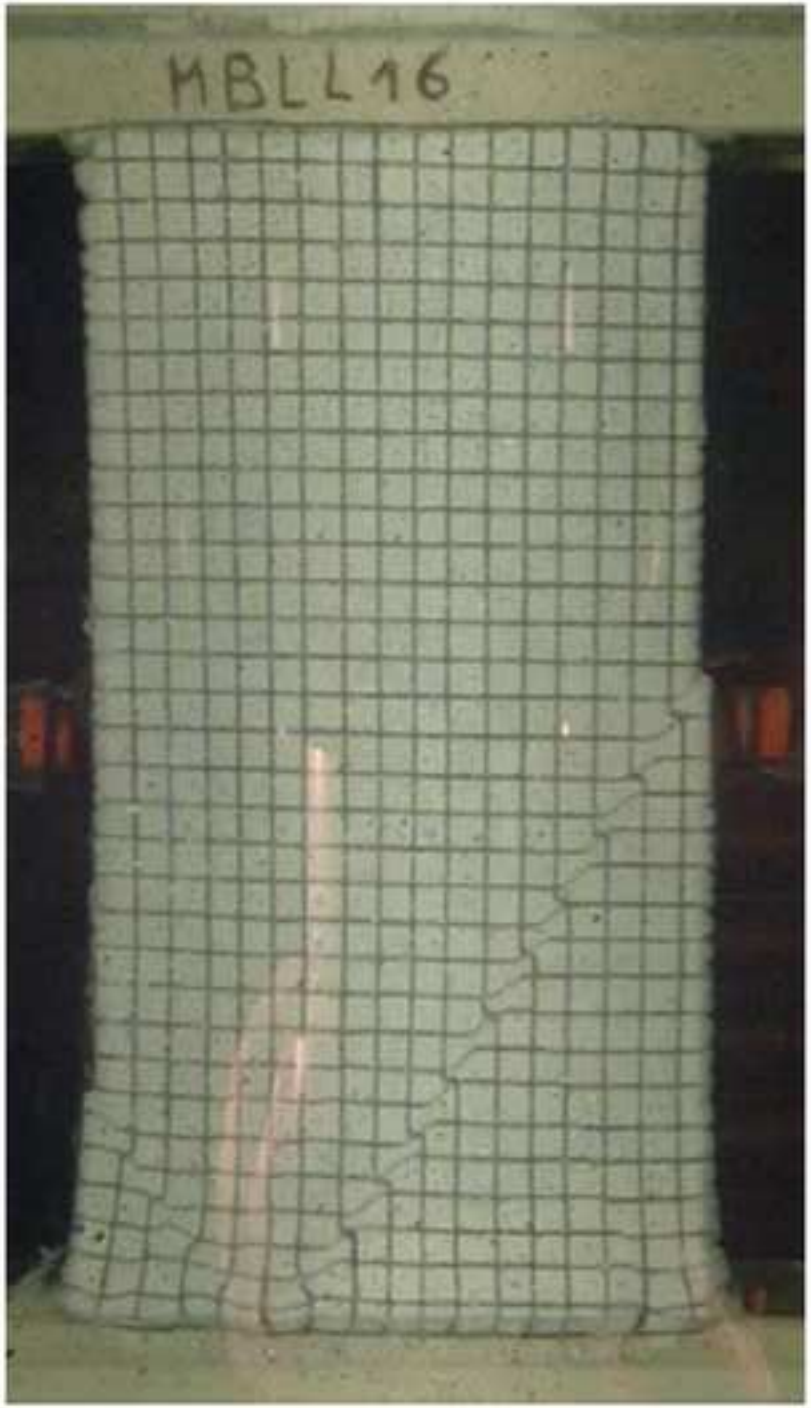

Figure 26

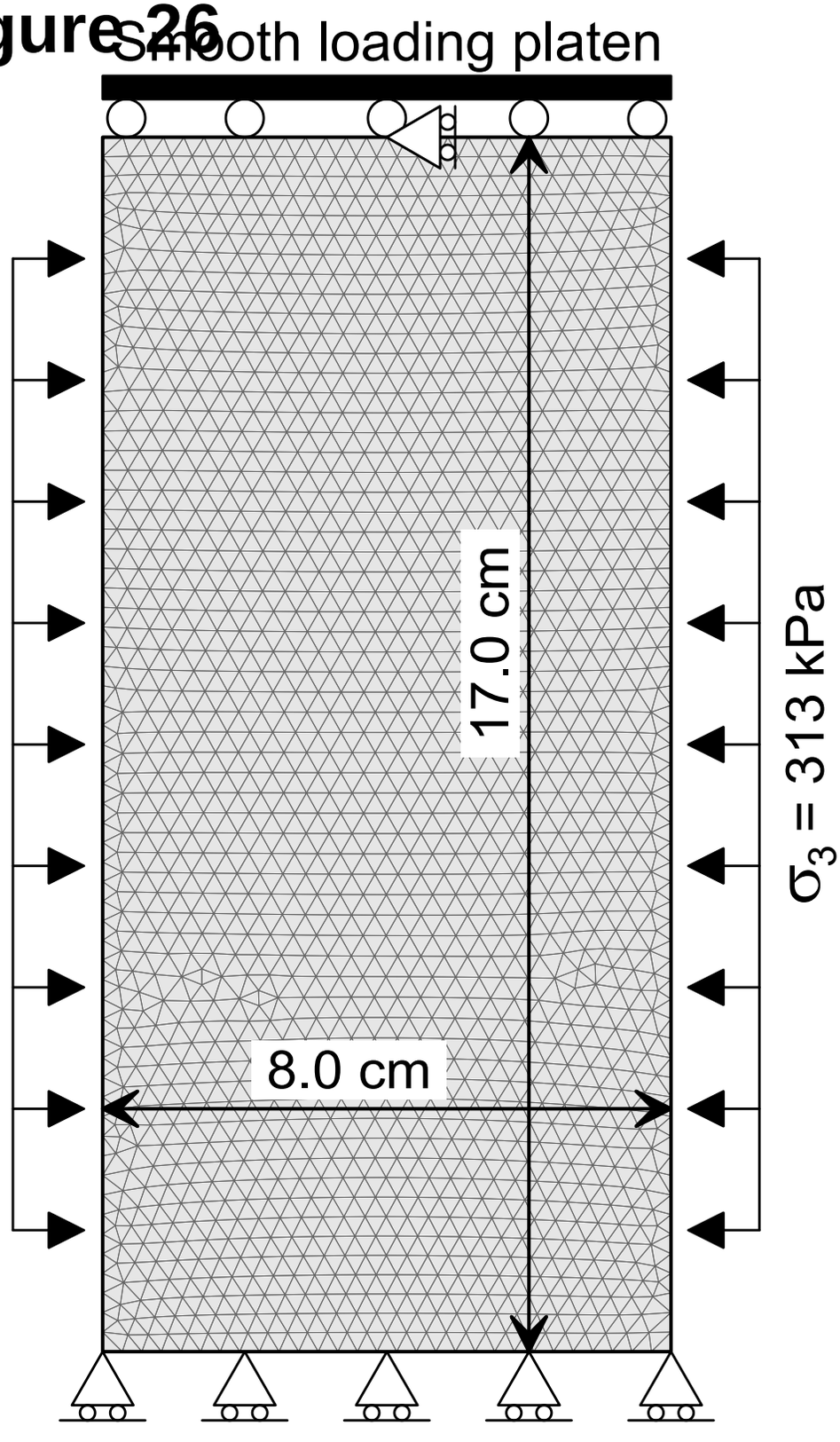
a)
Smooth loading platen
17.0 cm
8.0 cm
σ_3 = 313 kPa

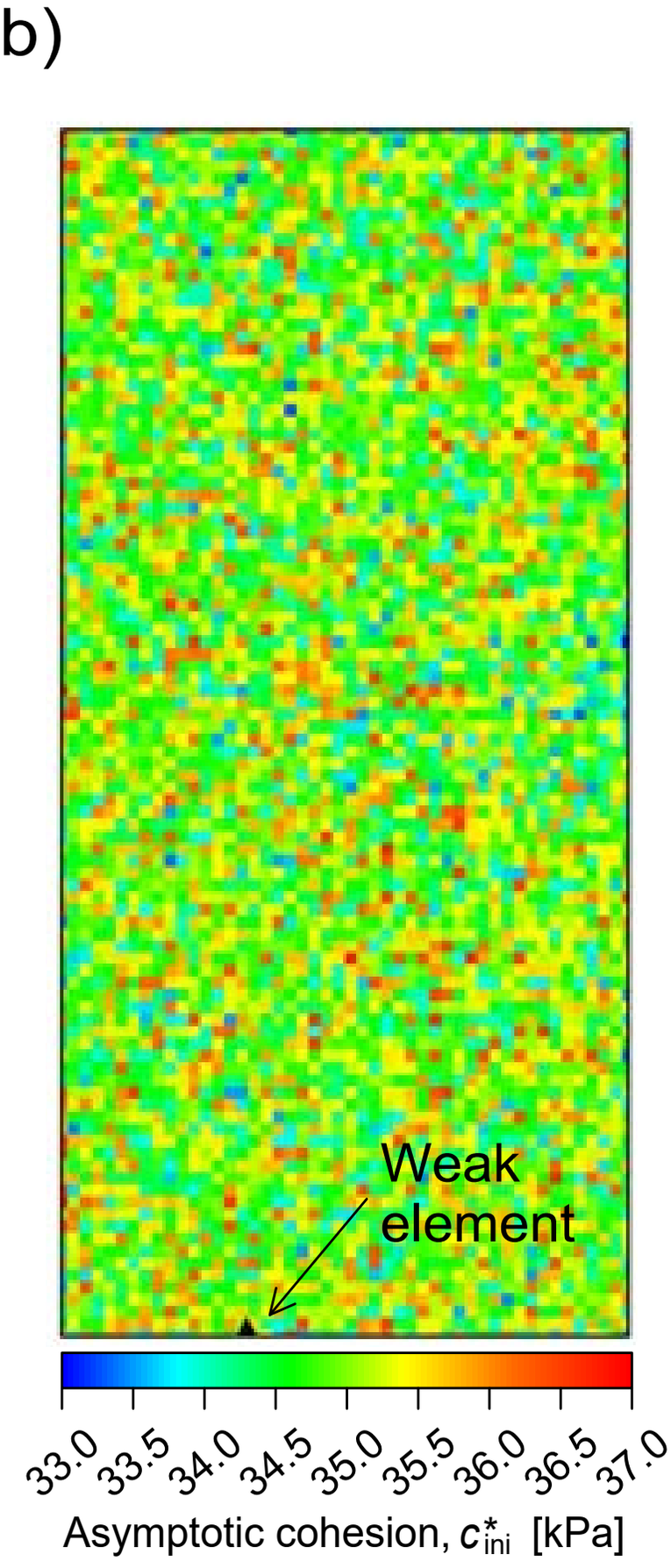
b)
Weak element
33.0
33.5
34.0
34.5
35.0
35.5
36.0
36.5
37.0
Asymptotic cohesion, c^*_{ini} [kPa]

Figure 27

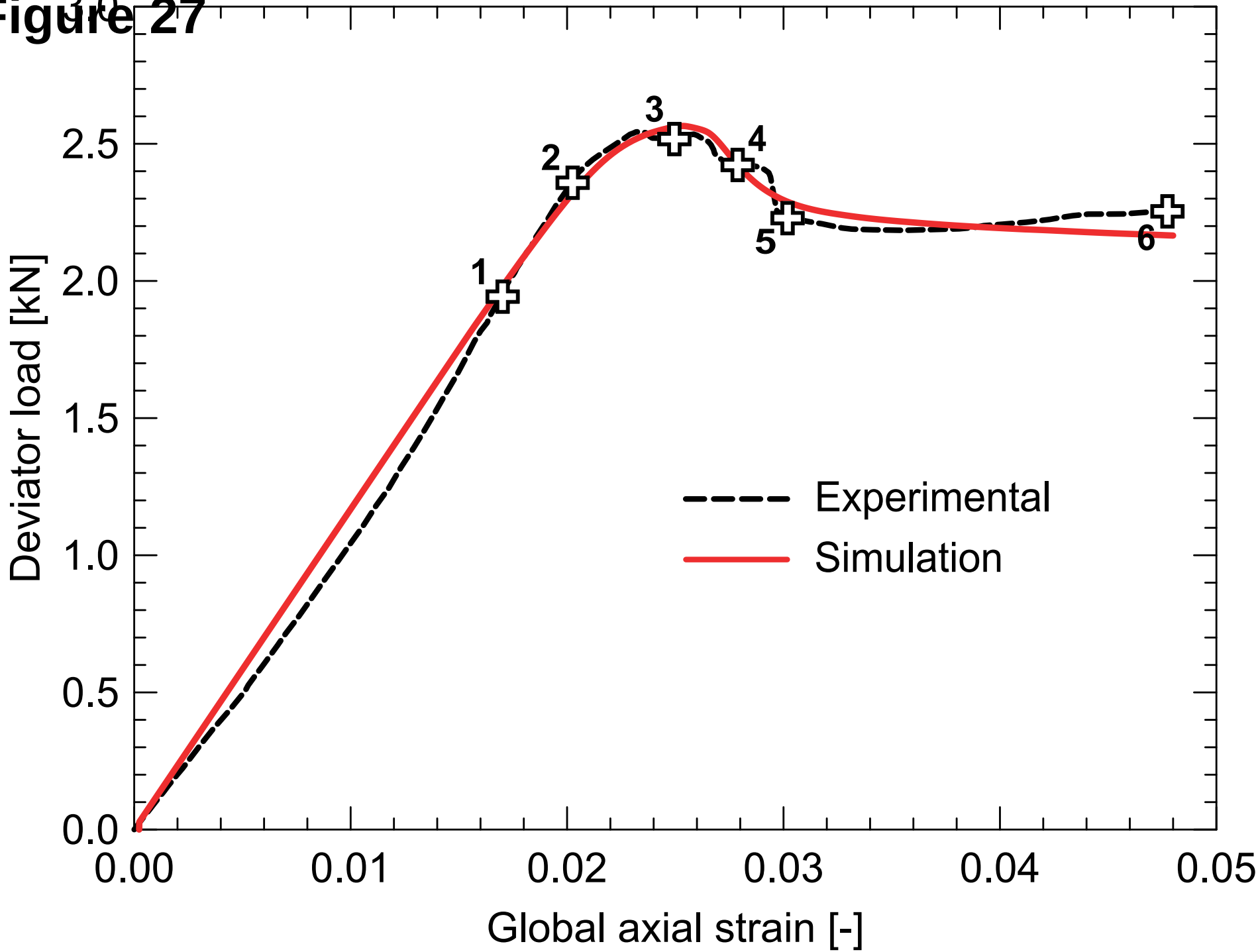
Deviator load [kN]
Global axial strain [-]
0.0
0.5
1.0
1.5
2.0
2.5
3.0
0.00
0.01
0.02
0.03
0.04
0.05
1
2
3
4
5
6
Experimental
Simulation

Figure 28